



Chair of Materials Physics

Master's Thesis

Probing local atomic strain of metallic  
glasses with nanometer resolution using  
TEM diffraction mapping

Julius Keckes, BSc

March 2022



**EIDESSTATTLICHE ERKLÄRUNG**

Ich erkläre an Eides statt, dass ich diese Arbeit selbständig verfasst, andere als die angegebenen Quellen und Hilfsmittel nicht benutzt, und mich auch sonst keiner unerlaubten Hilfsmittel bedient habe.

Ich erkläre, dass ich die Richtlinien des Senats der Montanuniversität Leoben zu "Gute wissenschaftliche Praxis" gelesen, verstanden und befolgt habe.

Weiters erkläre ich, dass die elektronische und gedruckte Version der eingereichten wissenschaftlichen Abschlussarbeit formal und inhaltlich identisch sind.

Datum 04.03.2022

---

Unterschrift Verfasser/in  
Julius Keckes

## **Danksagung**

Ich möchte mich an dieser Stelle bei all jenen bedanken, die mich während meines Studiums, sowie bei der Anfertigung dieser Masterarbeit betreut und unterstützt haben.

Zunächst möchte ich mich bei meinem Betreuer von Seiten der ÖAW, Dr. Christoph Gammer bedanken, der es mir ermöglicht hat eine Arbeit mit dieser interessanten Fragestellung zu verfassen. Danke für die zahlreichen detaillierten Gespräche über die Elektronenmikroskopie, Materialphysik und das Programmieren, sowie für die ausführliche Korrektur dieser Arbeit.

Ebenso gilt mein Dank an meinen Betreuer von Seiten der Montanuniversität, Prof. Dr. Jürgen Eckert, welcher durch sein tiefgreifendes Fachwissen zur Fertigstellung dieser Arbeit beigetragen hat.

Der größte Dank gebührt meinen Eltern Daniela und Jozef, die mich bereits mein gesamtes Studium unterstützt haben und mir in schwierigen Zeiten stets zur Seite standen. Danke für die langjährige finanzielle und emotionale Unterstützung, ohne die ich mir meinen Studienabschluss nicht vorstellen könnte.

Ein besonderer Dank gilt meiner Freundin Stefanie, die mir während meines Studiums stets zur Seite gestanden ist und mich auch vor anspruchsvollen Prüfungen mit motivierendem Beistand gestärkt hat.

Zum Schluss möchte ich mich bei all meinen Freunden, Kommilitonen und Wegbegleitern bedanken, die mir auch außerhalb des Studiums eine willkommene Ablenkung boten und emotionalen Rückhalt gaben.

## Zusammenfassung

In dieser Arbeit wird die Charakterisierung von metallischen Gläsern mittels Nanobeam-Elektronenbeugung (NBED), auch bekannt als vierdimensionale Rastertransmissionselektronenmikroskopie (4D STEM), unter Verwendung von Präzessions-Elektronenbeugung (PED) untersucht. Der Schwerpunkt liegt auf der Auswertung von Nanodiffraktionsdatensätzen durch Anpassung einer parametrischen Ellipsengleichung, die eine zweidimensionale Bestimmung lokaler elastischer Dehnungen, sowie eine Charakterisierung der Struktur und Zusammensetzung auf der Nanoskala ermöglicht. Es wird ein Einblick in die Implementierung des Anpassungsverfahrens, sowie in die Erfassung der Datensätze und die anschließenden Datenverarbeitungsschritte gegeben. Mit dem Ziel, die optimalen experimentellen Parameter und geeignete Auswerteeinstellungen zu bestimmen, wird eine Studie an einer Cu-Zr-Al-Legierung aus massivem metallischem Glas (BMG) durchgeführt, welche das Potenzial zur Abbildung intrinsischer struktureller Heterogenitäten von metallischen Gläsern (MG) aufzeigt. Die Methode wird auf eine nanostrukturierte  $(Co_{6.8\pm 3.9}Ta)_{100-x}B_x$  MG-Dünnschicht angewandt und zeigt eine räumliche Auflösung von wenigen Nanometern bei der Bestimmung elastischer Dehnungen, sowie der Charakterisierung von Struktur und Zusammensetzung, während sie gleichzeitig Einblicke in die Dehnungsverteilung und Struktur an amorphen Grenzflächen ermöglicht. Zusätzlich wird ein nanomechanisches in-situ Experiment an einem Cu-Zr-Al BMG Biegebalken durchgeführt, bei dem 4D STEM Datensätze erfasst werden. Eine anschließende Auswertung ermöglicht die Bestimmung lokaler mehrachsiger elastischer Dehnungsverteilungen, die bei unterschiedlichen Biegebelastungen auftreten und den Verlauf der Spannungskonzentrationen an der Kerbposition der Probe zeigen. Die Auflösung mit der die lokalen elastischen Dehnungen, die Struktur und die Zusammensetzung von MGs charakterisiert werden können, bietet Möglichkeiten für die Materialoptimierung, beispielsweise durch den quantitativen Vergleich von gewonnenen Ergebnissen mit Simulationen.

## Abstract

This thesis elucidates the characterization of metallic glasses (MGs) by means of scanning nanobeam electron diffraction (NBED) mapping, also known as four-dimensional scanning transmission electron microscopy (4D STEM), using precession electron diffraction (PED). An emphasis lies on the evaluation of nanodiffraction datasets through fitting of a parametric ellipse equation, which enables two-dimensional determination of local elastic strains, as well as structural and compositional characterization at the nanoscale. An insight is given into the implementation of the fitting procedure, as well as dataset acquisition and subsequent data processing steps. A study is conducted on a Cu-Zr-Al bulk-metallic-glass (BMG) alloy, to determine optimal experimental parameters and a suitable evaluation approach, while demonstrating the potential of mapping intrinsic structural heterogeneities of MGs. The method is applied to a nanostructured  $(Co_{6.8\pm 3.9}Ta)_{100-x}B_x$  MG thin film, proving the spatial resolution of a few nanometres for the determination of elastic strains, as well as structural and compositional characterization, while also allowing unique insight into strain distribution and structure at amorphous interfaces. Additionally, an in-situ nanomechanical testing experiment is conducted on a Cu-Zr-Al BMG bending beam, during which 4D STEM strain mapping datasets are acquired. A subsequent evaluation allows a quantification of local multiaxial elastic strain distributions, occurring at different bending loads, which indicate an evolution of the stress concentrations at the beam notch position. The unprecedented resolution with which local elastic strains, structure and composition of MGs can be characterized, enables opportunities for material optimization, such as the quantitative comparison of obtained results to simulations.

## Table of Contents

1.	Introduction .....	5
2.	State of the Art.....	7
2.1.	Overview of Metallic Glasses .....	7
2.1.1.	Composition.....	7
2.1.2.	Solidification of Metallic Melts .....	8
2.1.3.	Glass-Forming Ability .....	9
2.1.4.	Resistance to Crystallization.....	10
2.1.5.	Bulk Metallic Glasses.....	10
2.2.	Fabrication of Bulk Metallic Glasses.....	11
2.2.1.	Melt Spinning .....	11
2.2.2.	Water Quenching.....	12
2.2.3.	Copper Mould Casting.....	12
2.2.4.	Flux Melting .....	12
2.2.5.	Thermoplastic Forming of BMGs.....	13
2.3.	Synthesis of Thin Film Metallic Glasses.....	13
2.3.1.	Physical Vapor Deposition (PVD).....	13
2.3.1.1.	Vacuum Deposition .....	14
2.3.1.2.	Sputter Deposition .....	14
2.3.1.3.	Control of Thin Film Growth .....	16
2.3.1.4.	Ultrastable Metallic Glasses.....	20
2.3.2.	Annealing induced Amorphization.....	21
2.4.	Microstructure of Metallic Glasses.....	22
2.4.1.	Structure Models.....	22

2.4.1.1.	Random Packing of Spheres by J.D. Bernal .....	22
2.4.1.2.	Atomic Distribution Functions .....	23
2.4.1.1.	Modern Models of the Atomic Structure.....	25
2.5.	Characterization Methods .....	27
2.5.1.	X-Ray Diffraction Techniques .....	27
2.5.1.1.	Laboratory XRD Sources.....	27
2.5.1.2.	Synchrotron X-ray Diffraction .....	28
2.5.2.	Conventional TEM Techniques.....	29
2.5.2.1.	TEM Bright-field, Dark-field and Diffraction Mode .....	30
2.5.2.2.	High resolution TEM Mode .....	31
2.5.3.	Scanning Transmission Electron Microscopy .....	32
2.5.4.	Dark-Field STEM.....	32
3.	Implementation of the Evaluation Procedure.....	33
3.1.	Nanobeam Electron Diffraction in 4D STEM.....	33
3.1.1.	Formation of NBED Patterns.....	34
3.1.2.	Effect of Precession Electron Diffraction.....	35
3.1.3.	Recording of 4D STEM Maps.....	36
3.2.	Information Contained in NBED Patterns .....	37
3.2.1.	Ring Ellipticity.....	37
3.2.2.	Mean Ring Radius and Width.....	38
3.2.3.	Ring and Background Intensity.....	38
3.3.	Evaluation of NBED Patterns.....	39
3.3.1.	Parametric Ellipse Equation.....	39
3.3.2.	Technical Implementation of 4D STEM-Map Strain Evaluation.....	41

3.3.3.	Data Conversion and Frame Alignment.....	42
3.3.4.	Frame Pre-processing Steps.....	43
3.3.5.	Fitting Procedure.....	44
3.3.5.1.	Programmatic Implementation.....	45
3.3.5.2.	Multiprocessing Implementation.....	46
3.3.6.	Visualization of Fitting Results.....	47
3.3.6.1.	Calculation of Strains.....	48
3.3.7.	Virtual BF and DF.....	49
4.	4D STEM Parameter Study.....	50
4.1.	Experiment.....	50
4.2.	Evaluation.....	51
4.3.	Results and Discussion.....	52
4.3.1.	Discussion of the Influence of Scanning Parameters.....	52
4.3.2.	Discussion of the Influence of Fitting Parameters.....	54
4.3.3.	Conclusion I.....	56
5.	Strain Mapping on Multi-layered TFMG Samples.....	58
5.1.	Introduction.....	58
5.2.	Experiment and Evaluation.....	58
5.3.	Results.....	59
5.4.	Discussion.....	62
5.5.	Conclusion II.....	63
6.	In-situ strain mapping of a MG bending beam during loading.....	65
6.1.	Introduction.....	65
6.2.	Experiment.....	65



6.3. Evaluation.....	66
6.4. Results.....	67
6.5. Discussion.....	69
6.6. Conclusion III.....	69
7. Summary.....	71
8. References.....	72

## 1. Introduction

Metallic glasses (MG) are used in a variety of technical applications due to their unique physical properties. Whether as Bulk Metallic Glasses (BMG) in various macroscopic geometries, or on a micrometre scale, for example as precision gears in micro-electro-mechanical systems (MEMS). Due to the absence of an atomic crystal structure, many properties differ from those of metallic crystalline materials. The material class of MGs, sometimes also termed amorphous metallic alloys, excels with properties such as high tensile strength, corrosion and wear resistance and soft magnetic properties. With more sophisticated material applications, the demands on material properties are steadily growing. To enable controlled optimization of specific materials properties, advanced characterization techniques are needed that allow obtaining structure-property relationships. While multiple nanoscale characterization methods based on transmission electron microscopy (TEM) exist for crystalline materials, they cannot be straightforwardly applied to amorphous materials, due to their lack of a periodic structure.

Scanning nanobeam electron diffraction on the other hand does not require a periodic lattice for imaging and is therefore also applicable to amorphous materials. It allows the characterization of atomic structure, as well as composition and local elastic strains across amorphous materials with a nanoscale spatial resolution. In this thesis, a data evaluation procedure for 4D scanning transmission electron microscopy (STEM) datasets will be presented, conducted by fitting a parametric ellipse equation to nanobeam electron diffractograms. Firstly, the theoretical basis on MGs, their structure and characterization by TEM will be presented. Afterwards, a parameter study will be conducted, which identifies optimal scanning and acquisition parameters for capturing the 4D STEM dataset, as well as data processing and fitting parameters for a precise evaluation. In the following 4D STEM will be used to measure the local strain field in multi-layered nanostructured thin film specimens. Finally, to reveal the evolution of the strain field during deformation, 4D STEM will be applied to map a MG bending beam loaded in-situ. Two-dimensional maps are obtained revealing the local elastic strain distributions with a spatial resolution of a few nanometres, allowing to obtain an insight into scale of the most fundamental deformation processes. Simultaneously, 4D-STEM allows obtaining an information about the structure and composition of the

amorphous materials. The method can be used to map residual elastic strains as well as local transient strains evolving during mechanical tests on samples of a variety geometrical shapes, making it of general importance for a variety of applications [1].

## 2. State of the Art

### 2.1. Overview of Metallic Glasses

MGs are a class of metallic materials, which do not possess a regular arrangement of atoms. The first MG was discovered in 1960, when an alloy of  $\text{Au}_{75}\text{Si}_{25}$  has shown an amorphous structure, after a rapid solidification of the liquid melt [2]. Since then, many types of MGs with different properties have been synthesized for a multitude of technical applications. Due to the lack of translational symmetry or long-range ordering of atoms, no general nearest neighbor distance or coordination number can be defined. Consequently, a crystal lattice and its defects, such as grain boundaries or dislocations does not exist in MGs [3]. This inherent structural difference causes certain material properties of MGs to greatly differ from those of crystalline metals, such as a high elastic limit, high specific strength, hardness, good soft-magnetic properties, as well as corrosion and wear resistance [4]. It should be noted that the term MG is often differentiated from other types of non-crystalline metals. A metallic liquid melt, which is continuously cooled, yields a MG, while also being called non-crystalline. In contrast to this, non-crystalline metals which are synthesized by other techniques, such as mechanical alloying or physical vapor deposition, can be called amorphous metals [5]. However, this nomenclature is often not precisely followed, as amorphous alloys featuring a glass-transition temperature  $T_g$  are often labeled MG. The term MG can also arise from the classification of glasses into their chemical bond types. While “conventional” glasses such as Silicate, Chalcogenide or Halide glasses show interatomic bonds that exhibit characteristics of covalent and ionic bonds, non-crystalline metals show a metallic bond character and are thus termed MGs [6].

#### 2.1.1. Composition

For technological applications, MGs are formed in a multi-component system. The reason for this is primarily dictated by the thermodynamics and kinetics of solidification. In order to obtain pure amorphous metals, the fast nucleation and growth kinetics of crystallization would require very high cooling rates, which are not achievable with current quenching techniques. There already have been multiple successes in forming amorphous phases in pure metals through ultrafast quenching of metallic melts, achieving cooling rates of up to

$\frac{10^{14}K}{s}$  [7]. Such cooling rates are however infeasible at a larger scale, which is the reason for requiring alloy systems to form MGs. All glass-forming alloy systems can be classified into either consisting only of metallic components (metal-metal  $M_I$ - $M_{II}$  types) or metallic components and non-metallic components (metal-metalloid  $M$ - $NM$  types). Both metal and metalloid contents can be represented by a single type of atom or a combination of different atoms [8]. An example for a metal-metal type MG would then be  $Zr_{65}Al_{7.5}Ni_{10}Cu_{17.5}$ , an exemplary metal-metalloid type MG is  $Pd_{40}Ni_{40}P_{20}$  [3].

### 2.1.2. Solidification of Metallic Melts

When lowering the temperature of a metallic melt under its melting point  $T_M$  (or equilibrium freezing temperature  $T_f$ ), the liquid becomes undercooled. This undercooling promotes the formation of crystallization nuclei, which form at heterogeneous nucleation sites through thermal fluctuations. From a thermodynamical point of view, the undercooling is necessary to overcome the activation energy required for stable nuclei to form. After a nucleus with a critical size has formed, crystal growth can take place, at the end of which the liquid melt has solidified into a crystalline solid. When considering melts of MGs, the formation of a critical nucleus for crystallization is inhibited mostly through using high cooling rates. Consequently, the liquid can be undercooled to a higher degree, without crystallization occurring (while being in a supercooled state). With an increasing amount of undercooling, the viscosity of the liquid increases, while its volume decreases, which in turn reduces atomic mobility. Under a certain temperature, the atomic mobility is limited to such a degree, that even if a critical nucleus could form, crystallization would not be possible, thereby the liquid becomes “frozen-in” [3]. In this temperature region, the viscosity reaches values of around  $10^{12}$  Pa\*s, the corresponding temperature is called glass-transition temperature  $T_g$ . With a faster cooling rate during solidification, the glass transition temperature rises. This indicates, that  $T_g$  is dependent on the kinetics of the solidification, dictated by cooling rate and undercooling, meaning that the glass transition is a kinetic transition, not a thermodynamic phase transformation [5].

### 2.1.3. Glass-Forming Ability

The Glass-forming ability (GFA) of an alloy indicates the suitability of the particular alloy for the formation of a glassy phase through continuous cooling of the liquid melt. It is defined as the slowest cooling rate, which can be applied to the melt, in order to solidify it in a glassy state, without any crystallization. This critical cooling rate  $R_c$  can be experimentally measured through the construction of time-temperature-transformation ( $T-T-T$ ) diagrams [5]. The lower the critical cooling rate, the higher the GFA of an alloy, since crystal formation is suppressed even at lower cooling rates. The cooling rate is however difficult to measure precisely, thus other ways have been found to quantitatively estimate the GFA of an alloy. There are numerous approaches to calculating the GFA, most of them use temperatures such as the glass-transition temperature  $T_g$ , liquidus temperature  $T_f$  and onset crystallization temperature  $T_x$  [9]. A simple approach involves calculating the reduced glass-transition temperature, which is calculated as  $T_{rg} = \frac{T_g}{T_f}$  and correlates with the critical cooling rate  $R_c$  for glass formation. During solidification, the formation of crystals in the liquid is possible starting from the liquidus temperature  $T_f$ , until the glass-transition temperature  $T_g$ . The smaller this temperature window, the easier it is to suppress crystallization, indicated by a high reduced glass-transition temperature  $T_{rg}$  [3]. Another approach involves calculating the difference between crystallization temperature and glass-transition temperature as  $\Delta T = T_x - T_g$ . When considering a multi-component system,  $T_f$  and  $T_g$  are dependent on the composition of the system. While  $T_g$  only changes slightly with composition, the liquidus temperature shows a strong dependence in most cases. This is especially the case when considering “deep” eutectics, which are eutectic points that show a strong liquidus temperature decrease at the eutectic composition, in comparison to the melting points of the individual components. When approaching the eutectic composition, the liquidus temperature decreases, which leads to a smaller region in which crystallization can occur. At the eutectic point, the liquidus temperature is at its minimum, which causes a maximum reduced glass-transition temperature  $T_{rg}$ . Therefore it can be stated that multicomponent systems with deep eutectics are suitable candidates for glass-forming systems with a high GFA [3].

### 2.1.4. Resistance to Crystallization

Besides the previously described GFA, another important criterion which needs to be considered for the technical application of MGs, is the resistance to crystallization of the glassy state. The resistance to crystallization describes the thermal stability of the glass. When raising the temperature of a MG above the glass-transition temperature, crystallization will start at the above-mentioned crystallization temperature  $T_x$ . This temperature is therefore a measure for the stability for the glass, a higher  $T_x$  yields a more thermally stable glass. This alone is however not the sole indicator for the thermal stability, since also the stability of the liquid phase needs to be considered. The stability of the liquid phase can be estimated with  $\frac{1}{2}(T_g + T_l)$ , with a lower value indicating a more stable liquid phase [5]. The stabilities of both phases are now combined into a parameter  $\gamma$ , representing a GFA as follows [9]:

$$GFA \propto \gamma = \frac{T_x}{T_g + T_l} \quad (1)$$

### 2.1.5. Bulk Metallic Glasses

Bulk metallic glass (BMG) is a term used for alloy systems, which show solidification into a glassy state at low critical cooling rates of 1 to 100 K/s. Without the need for ultrafast quenching, MGs can be obtained in larger dimensions than otherwise possible. While high critical cooling rates only allow the formation of MGs in the form of thin ribbons with low thickness, the low cooling rates of BMGs enable solidification of thicker geometries ranging from one millimetre up to several centimetres of thickness, while being entirely amorphous [5]. BMGs are multicomponent alloy systems, which exhibit deep eutectics, leading to a high  $T_{rg}$  and consequently low critical cooling rates. The ability of BMGs to solidify in thicker geometries, is often described by the maximum diameter that a rod of a particular BMG can be solidified to, while still being in a fully glassy state. In order for a BMG to form, three empirical rules need to be fulfilled, as formulated by Inoue [10]:

1. The alloy must contain at least three components. Lower critical cooling rates are needed to obtain a glassy state, as more alloying elements generally shift the curve for crystallization in a  $T$ - $T$ - $T$  diagram to the right. The formation of a glassy state thus becomes easier, with more components in a system.

2. The main three elements of the system should have a significant atomic size difference of at least 12%.
3. The main three elements should have a negative heat of mixing.

These rules resemble the requirements for the formation of a eutectic point. This results in a clear connection between the formation of eutectic points and the solidification of BMGs in such multicomponent systems. The second and third rule are responsible for the formation and efficient packing of atomic clusters, which lead to decreased atomic mobility in the supercooled state and thus inhibit crystallization [5].

## **2.2. Fabrication of Bulk Metallic Glasses**

As described in the previous chapter, the main challenge in producing conventional MGs, is achieving a sufficiently high cooling rate. This requirement was met by various rapid solidification processing (RSP) techniques, which enabled further advancements in the synthesis of new MG alloys. Likewise, the discovery of the exceptional properties of MGs, fostered further advances in RSP techniques. The high number of developed RSP techniques, enable cooling rates beginning at  $\frac{10^4 K}{s}$  and going even higher [11]. RSP techniques focused on MGs, involve melting the material using a certain heating method, followed by bringing a small portion of material in contact with a heat sink. The contact between the melt and a thermally conductive surface (e.g., Copper) leads to a fast heat extraction and enables high cooling rates. With the development of BMG alloys, the requirement for high cooling rates could be partially avoided, since cooling rates of 1 to 100 K/s were sufficient to suppress nucleation of crystallites. This enabled the use of a multitude of casting methods, producing various geometries of solidified BMGs [12]. Similarly, water could now be used as a quenching agent, enabling a simpler approach to producing BMGs ingots with diameters of up to 72 mm [13].

### **2.2.1. Melt Spinning**

In the course of the RSP advancement and the synthesis of new MG alloys, melt spinning has been the predominant method for fabrication of continuously solidified ribbons. In this process, the alloy is melted in a crucible, using inductive heating, and then ejected through a nozzle at the lower end of the crucible. In the so-called chill-block melt-spinning (CBMS)



technique, the molten alloy comes into contact with a cooled and rotating metallic disk, acting as a heat sink. The direct contact between the metallic surface and the melt, results in a fast heat transfer, which leads to solidification of the melt into a thin glassy ribbon. After a short distance in contact with the spinning disc, the ribbon loses contact through centrifugal force. This method allows high solidification rates of up to  $10^6$  K/s [14].

### **2.2.2. Water Quenching**

The simplest method to obtain BMGs, is based on using water as a quenching agent. The alloy is first melted inside a container using induction melting. A quartz tube is most often used as a crucible, but chemical compatibility between the molten alloy and the crucible needs to be considered. The container holding the molten alloy is then quenched using water. Achievable cooling rates are in the range of  $10^2$  K/s, which lead to formation of BMGs with comparatively little residual stress [5].

### **2.2.3. Copper Mould Casting**

In this method, the alloy is melted using either induction heating of a crucible or arc melting, in an inert atmosphere. The melt is then poured into a cooled copper mould, either under air or inert atmosphere. Due to the intimate contact between melt and copper surface, a fast heat extraction is possible, leading to a suppression of crystallization during solidification. Possible modifications of this method include high-pressure die casting, suction casting and several others. These methods generally employ a pressure differential to accelerate the filling of the casting chamber and thus increase solidification rates and productivity [5].

### **2.2.4. Flux Melting**

The GFA of an alloy is significantly influenced by the nucleation process during solidification. If heterogeneous nucleation was to be suppressed entirely, much lower solidification rates could be used to obtain an amorphous structure, since crystal formation is only dictated by the homogeneous nucleation rate. The flux melting technique enables the removal of impurities, which act as heterogeneous nucleation sites. The process starts by melting the fluxing agent, for example  $B_2O_3$ , together with the metallic alloy inside a crucible. After melting, the content of the crucible is cooled to a temperature, at which the fluxing agent is still in the liquid state. This temperature cycle is repeated multiple times, during which

impurities from the alloy migrate into the fluxing agent. This technique yields an alloy with a strongly enhanced GFA, due to suppression of heterogeneous nucleation of crystallites during solidification. Fluxed specimens can thus be solidified into a glassy state in considerably larger geometries, compared to non-fluxed alloys [15].

### **2.2.5. Thermoplastic Forming of BMGs**

BMGs show physical properties of a metastable liquid with high viscosity in the supercooled liquid region, which lies between  $T_g$  and  $T_x$  of the material. This property is used for a fabrication technique termed thermoplastic forming, where the BMG can be freely formed with high precision and similar process parameters to plastics. The technique can be used to form BMGs in complex geometries on a micrometre scale, which is ideal for application in MEMS [16].

## **2.3. Synthesis of Thin Film Metallic Glasses**

A distinction can be maintained between MGs glasses fabricated by continuously cooling of a metallic melt and other types of amorphous metals, synthesized by other techniques. Selected synthesis methods for amorphous metallic thin films, also labelled thin film metallic glasses (TFMGs) will be described in this chapter. Most of the synthesis approaches involve raising the free energy of the system using a various methods and afterwards quenching the material, with the goal of obtaining an amorphous structure [5].

### **2.3.1. Physical Vapor Deposition (PVD)**

PVD is a synthesis technique used for growing thin films with varying properties and morphologies on a substrate. This is achieved by vaporizing a source material, using different methods of energy input. After a transport phase of the vaporized atoms or molecules through a vacuum or low-pressure gas atmosphere, a certain amount of the material condenses on the substrate. Additionally, in reactive deposition processes a chemical reaction takes place between the vaporized material and the gas atmosphere to form a chemical compound. Under certain process conditions, PVD can be used to synthesize TFMGs. Due to the high cooling rate of condensing vapor on a solid substrate, thin films can be grown far from thermodynamic equilibrium, often farther than possible through quenching of a liquid melt. With appropriate deposition parameters such as temperature, composition and

inert gas pressure, the condensing vapor forms a layer on the substrate, without any crystallization occurring. PVD processes can be categorized by the method of energy input, which is used to form the initial vapor phase of the source material [17].

### **2.3.1.1. Vacuum Deposition**

In this type of PVD process, thermal evaporation is used to generate a vapor of the source material. The necessary heat input is achieved through heating a wire coil using electric current, also called resistance heating. Heat input is also achievable using an electron beam or laser beam. The resulting high temperatures cause a rise in the vapor pressure of the material, through which the atoms or molecules of the source material begin to sublime. After leaving the surface of the material, the atoms or molecules travel through the vacuum chamber. Once the particles come in contact with the lower-temperature substrate, they transfer a part of their heat energy to the substrate and condense [17].

### **2.3.1.2. Sputter Deposition**

Instead of using thermal energy for vapor generation, this process is based on the transfer of kinetic energy from a particle bombardment to atoms of the source material to generate the vapor phase. The basis for all sputter deposition processes is the glow discharge or plasma, in which current flows through a partially ionized gas with different degrees of ionization. First, the working gas, for example Argon, is introduced into the deposition chamber with a certain pressure and is then ionized by applying a certain voltage to the installed electrodes, which produces an electric field. During regular operation, the source material is used as the cathode and the substrate as the anode. The resulting “free” electrons and ions are then accelerated towards the corresponding electrodes in the electric field. The electrons can ionize additional gas atoms on their way to the anode through impact ionization, which is important for maintaining the glow discharge. The positively charged ions of the working gas are accelerated towards the cathode target, which consists of the source material. Upon impact of the gas ions, a transfer of kinetic energy onto atoms of the target material can take place. Depending on the ratio between transferred kinetic energy and the surface binding energy of the target atom, the atom can be ejected from the target material. After the sputtering process, a certain part of all sputtered atoms will then impact on the substrate, where the thin film is formed.

### **Magnetron Sputtering**

Magnetrons are employed in most sputtering processes and facilitate high deposition rates, as well as a low operating pressure of the sputtering gas. In this process, permanent- or electromagnets are placed under the target material, which introduces a magnetic field. The electric field caused by the application of DC or RF voltage, as well as the magnetic field from the magnetrons are now both used to influence the path of electrons in the plasma. Under all circular targets in the deposition chamber, an annular-shaped magnet is positioned on the outer edge of the target, while another magnet is located in the centre, having opposite polarity. The magnetic field lines thus form an arch beginning at the centre of the target and ending at its outer edge. The motion of electrons is strongly influenced by the acting Lorentz force, causing a helical trajectory above the area of the target. Electrons are mostly present in the region, where magnetic field lines are lying perpendicular to the electric field, which is the top of the magnetic field line arch. In this so-called ionization region, electrons are mostly confined, resulting in a glow discharge with the highest intensity and thus highest degree of sputtering. In addition to a balanced magnetic configuration, in which magnetic field lines form an arch originating in the centre of the target and passing to the outer border, two unbalanced variants exist. Unbalanced type I is a magnetic design, in which the central magnet possesses a stronger magnetic flux, than the annular magnet, resulting in all field lines originating in the centre, but not all closing in the annular magnet. In this configuration, the plasma is not strongly confined to the target area anymore. Unbalanced type II describes a configuration in which all field lines originate from the annular magnet but not all pass into the central magnet. This configuration allows the plasma to root out in direction of the substrate, causing a higher ion current density in the substrate region. In this design, ion bombardment of the substrate is possible during film growth, regulated using a substrate bias voltage [18].

### **Direct Current (DC) Sputtering**

The simplest practical form of the sputtering process is called direct current (DC) sputtering. During deposition, direct current with a high voltage is applied between the electrodes, which causes an ionization of the sputtering gas. The resulting positive gas ions are accelerated towards the negatively charged target surface, where they transfer their kinetic

energy onto the target atoms. The sputtered atoms then form the thin film on the positively charged substrate. The main drawback of this method, is that non-conductive source materials can't be sputtered, as an electric charge build-up would occur over time, which would compensate the applied DC voltage [19].

### **Radio Frequency (RF) Sputtering**

To remedy this issue, radio frequency (RF) sputtering can be used. The applied voltage and thus the electric field is now alternating with a high frequency, causing an alternating motion of the charged gas ions and electrons. Because of its lower mass, the electrons in the plasma are bombarding the target with a much higher intensity than the heavier ions, leading to a negative charge on the target surface. The resulting negative "self-bias" voltage on the target, accelerates the positive ions onto the target, leading to sputtering of the target atoms. Another effect of RF-sputtering is the increased collision probability between electrons and ions in the plasma, which allows the gas pressure in the sputtering chamber to be lowered significantly, while still sustaining the glow discharge [19].

### **Ion-Beam Assisted Deposition**

The Ion-Beam Assisted Deposition (IBAD) technique is often used in the synthesis of MG thin films. The difference of this process to a conventional magnetron sputtering or evaporation setup, is the use of one or multiple ion sources. During film growth, ion bombardment of the substrate and target area occurs, which influences the thin film growth process. Thin films deposited using IBAD, show better adhesion to the substrate, while the ion bombardment can enhance surface mobility of adatoms on the substrate.

#### **2.3.1.3. Control of Thin Film Growth**

During the PVD process, film growth is governed by various process parameters. Due to the broad range of parameters such as deposition temperature and working gas pressure, growth conditions far from thermodynamic equilibrium are possible. PVD deposition can therefore produce single-crystalline (epitaxial) films, as well as polycrystalline and amorphous films.

The process of polycrystalline film formation begins with the condensation of atoms of the target material on the substrate. The condensed and adsorbed adatoms possess a certain

surface diffusion rate, through which more atoms can accumulate to form islands. Islands represent single-crystalline nucleation sites for film growth. Similar to a liquid melt, impurities or defects represent low-energy-sites, at which island formation starts preferably. After the islands have formed, a further island growth can take place, during which the islands grow in size, until neighbouring islands impinge on each other, initiating the coalescence of islands. This phase is equivalent to a coarsening (ripening) process, in which the total island density decreases, until island boundaries can no longer move due to large grain sizes. Coalescence proceeds through grain boundary motion, as well as diffusion of surface atoms, with the aim of minimizing the total surface energy. Low-energy islands grow at the expense of high-energy islands, equivalent to grain growth. In the resulting structure, single-crystalline islands are representing grains, which form a polycrystalline film [20]. After formation of this initial film thickness of approximately 100 angstroms [18], the film can continuously grow in thickness (Figure 1).

Numerous modifications of process parameters can be carried out, in order to influence the film growth behaviour, for instance suppressing crystallization for the synthesis of TFMGs. In order to summarize the broad spectrum of deposition parameters, structure zone models (SZM) are often generated and used to show microstructural evolution as a function of process parameters.

### **Reduced Temperature**

An exemplary SZM (Figure 2) shows film microstructure of elemental crystalline materials depending on the reduced temperature of  $T_s/T_m$ , where  $T_s$  is the deposition temperature (or the substrate temperature) and  $T_m$  is the melting point of the target material [21]. The reduced temperature range is divided into multiple zones, in each of which the grown film shows certain microstructural features. At very low reduced temperatures ( $0 < T_s/T_m < 0.2$ ), film growth occurs in zone I, which is far from thermodynamic equilibrium. Since the surface mobility of adatoms is mainly governed by the substrate temperature, a lower reduced temperature limits the ability to form and grow islands in a given timeframe. The resulting low adatom mobility results in a microstructure consisting of crystalline fibres, which grow continuously from the initial nuclei. The adatoms are incorporated into the fibres at their

impact point. Due to this continuous growth, the lateral size, as well as the crystalline orientation are identical to the nuclei.

At higher reduced temperature ( $0.2 < T_s/T_m < 0.4$ ), denoted by zone T, adatom surface mobility is higher, leading to a competitive growth process of columnar crystals with differing crystallographic orientations. With growing film thickness, crystals with energetically favourable orientations grow laterally, due to the rising mobility of grain boundaries, which results in the formation of a textured polycrystalline structure.

The next zone is labelled zone II ( $0.4 < T_s/T_m$ ), in which grain boundaries have a high mobility. Due to this mobility, structural changes which reduce the surface and interface energy can take place. Through grain boundary movement, a coalescence of the initially formed nuclei is possible, followed by grain coarsening at higher temperatures. The resulting columnar crystals have a larger lateral size and possess similar crystalline orientation.

The conclusion from this SZM for the deposition of TFMGs is, that deposition conditions which suppress crystallization are generally achieved under low reduced temperatures, since this corresponds to a high quenching rate. The low mobility of adatoms thus hinders the formation of nucleation sites, which would initiate crystallization.

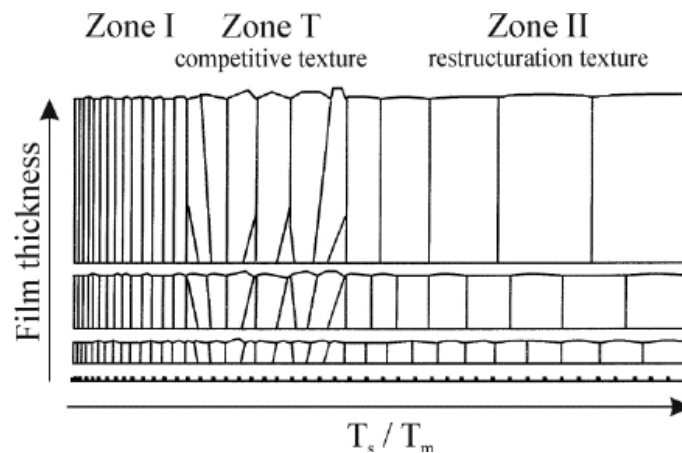


Figure 1: Barna and Adamik structure zone model of a polycrystalline film [21]

Similarly, Thornton's zone model for magnetron sputtering [22] predicts the structure of a thin film, grown under certain substrate temperatures and inert gas pressures. Each

structural zone possesses a dominating physical process, which controls the resulting structure and surface morphology (Figure 2).

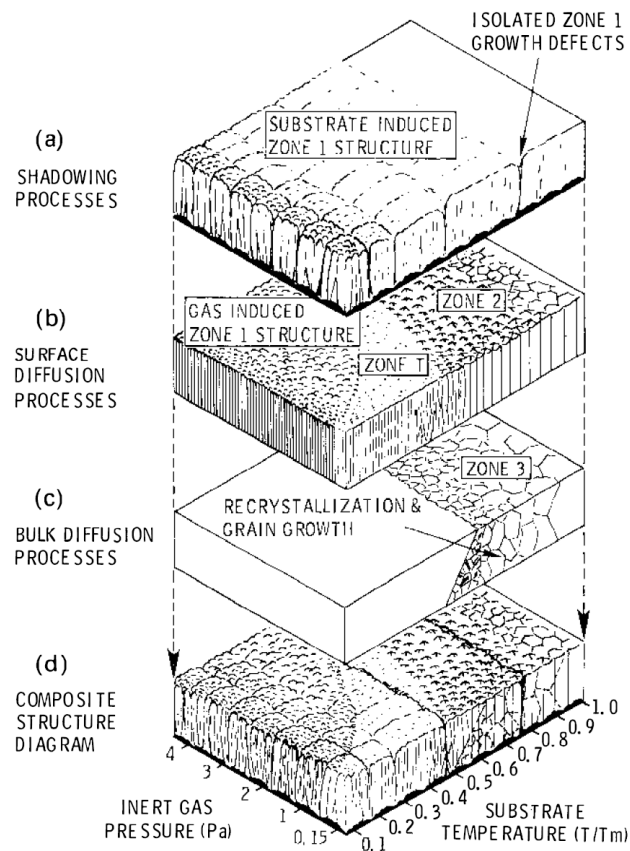


Figure 2: Thornton's structure zone model showing a superposition of physical processes [22].

As with the SZM by Barna and Adamik, an amorphous structure is predicted at low homologous temperatures  $\frac{T}{T_m}$ , at which adatom mobility is very low. After condensing the substrate surface, the adatoms do not possess sufficient mobility to move significant distances from their impingement point, thus hindering crystal formation.

### Thin Film Composition

In order to synthesize TFMGs, nucleation and crystal growth needs to be prevented after the condensation of the vapor phase. Considerably higher cooling rates are achievable in deposition processes, than through quenching of metallic melts. While this allows a broader range of metallic alloys to be solidified in an amorphous structure, the condensed vapor phase should have a precisely regulated composition. The composition can be controlled in a sputter deposition process using a variety of approaches. Considering for example MG



formation in the Zr-Cu system, co-sputtering can be employed, using two separate targets consisting of the metallic elements. In order to tune the film composition to a certain value, the deposition rates of the individual targets need to be known. The deposition rate of a target is often specified in  $\mu\text{m}/\text{h}$  and primarily controlled by the electric current density on the target during deposition. Raising the electric current on a target raises the intensity of the particle bombardment and thus the ejection of target atoms. The deposition rate is also strongly dependent on the target material, with heavier elements having a lower deposition rate overall. Therefore, deposition rates depending on electric current for all targets have to be known when tuning the film composition.

Another possibility for obtaining a suitable composition of MG alloys is employing single target sputtering, in which the used target already consists of the proper composition necessary to synthesize a TFMG.

#### **2.3.1.4. Ultrastable Metallic Glasses**

A recent discovery in MG fabrication are amorphous materials with very high thermodynamic stability against crystallization, termed ultrastable metallic glasses. The first ultrastable glasses were organic in nature, with exceptional thermodynamic stability and mechanical properties and synthesized through vapor deposition. Recently also certain alloy systems, such as Zr-Cu-Al, were used to produce ultrastable metallic glasses. The resulting solid showed improved properties such as higher glass transition temperature, as well as enhanced strength and hardness. The typical approach for synthesizing ultrastable metallic glasses is through single-target magnetron sputtering, typically using a high substrate temperature close to the glass transition temperature of the glass  $T_{sub} = 0.8 - 0.9T_g$  [23]. Together with a low sputtering rate, condensing atoms have a higher surface mobility. This gives the atoms enough time to form a more stable structure, than with regular deposition parameters [24]. Current experiments also show, that ultrastable metallic glasses are obtainable even under lower substrate temperatures  $T_{sub} \approx 0.43T_g$ , which is usually equal to room temperature. At low temperatures, the deposition rate  $R$  becomes a very important factor, with smaller values leading to higher glass transition temperatures and leveling off at around  $R = 1 \text{ nm min}^{-1}$  (Figure 3) [23].

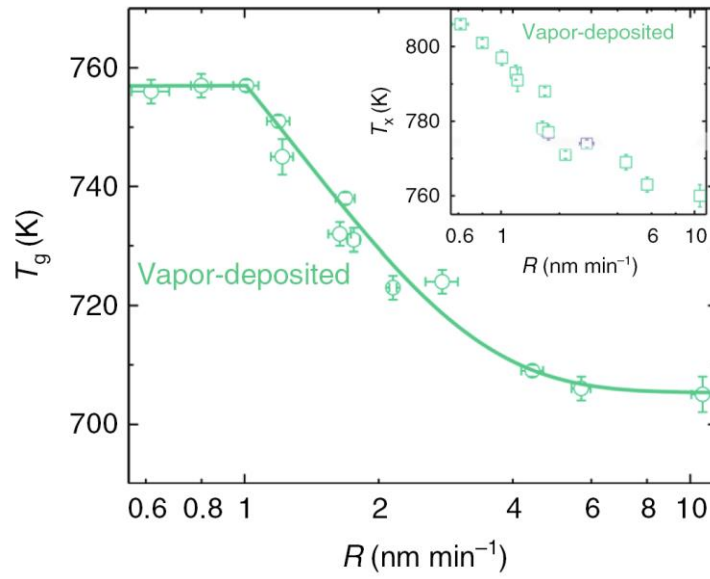


Figure 3: Dependence of the glass transition temperature  $T_g$  on the sputtering rate  $R$ , adapted from [23]

### 2.3.2. Annealing induced Amorphization

Certain multicomponent TFMG systems can be sputtered to form a metastable nanocrystalline structure at room temperature, for example in the Zr-Cu-Al-Ni system. This thin film is then transformed into an amorphous structure by annealing at a temperature, which lies in the supercooled liquid region  $\Delta T$ , between the glass transition temperature  $T_g$  and the onset of crystallization temperature  $T_x$ . At lower annealing temperatures, the obtained structure shows smaller, dispersed crystallites or crystalline networks in an amorphous matrix, yielding a higher hardness. Annealing at higher temperatures in the  $\Delta T$  range produces a fully amorphous structure, leading to a decreasing hardness and a strong increase in electrical resistivity. Raising the deposition temperature above the crystallization temperature  $T_x$  leads to an expected formation of nanocrystals. The changes in film structure and ratio of nanocrystallites can be used to adjust mechanic and electric properties of the thin film [25].

## **2.4. Microstructure of Metallic Glasses**

MGs are amorphous, since they do not possess a long-range ordering of atoms and translational symmetry. Their atomic arrangement is however not completely random, since a short-range order (SRO), medium-range order (MRO) and even a long-range topological order (LRT0) can be found in certain alloy systems. The SRO describes the arrangement of atoms in the region of the nearest neighbours of a reference atom, while the MRO considers a larger environment, usually including the second or third nearest-neighbours of the considered atom. LRT0 is a recently discovered [26] kind of ordering, in which a large region of the amorphous MG is topologically equivalent to the crystalline structure of the material, while the structures only differ in bond length and bond angles. As the MG is being loaded under pressure, the material is able to uniformly transform into a single crystal, which persists after unloading.

Amorphous solids also do not possess distinctly identifiable crystal structures. Crystal structures can in theory be fully described by its lattice vectors, yielding the 14 Bravais lattices and together with symmetry operations amounting to 230 space groups. A phase transition between two crystalline phases is also clearly detectable via different characterization methods. Amorphous structures on the other hand, have far more degrees of freedom, with a seemingly infinite number of indistinguishable configurations.

### **2.4.1. Structure Models**

To describe the amorphous structure of MGs, structure models were developed. Structure models are primarily based on structure information gathered from different kinds of experiments, as well as computer simulations, such as Monte Carlo simulations or molecular dynamics simulations [27].

#### **2.4.1.1. Random Packing of Spheres by J.D. Bernal**

A notable step in describing the atomic or molecular structure of a liquid, was performed by J.D. Bernal [28] in the 1960s. Through several iterations, physical models were assembled, with the aim of representing the ideal structure of a liquid. The first model was a spoke and ball model of an amorphous structure, later a random hard sphere model was made, consisting of a large number of painted steel ball bearings placed in a box. Through evaluating

the contact points of individual balls, a relationship was found throughout the entire model. It was possible to define several types of clusters, formed by the packing of the spheres, which are described by certain types of polyhedra [29]. According to the model, the random packing of spheres is made up by five different kinds of polyhedra (Figure 4), which can be packed together in an unlimited number of ways [30]. While the tetrahedron and octahedron are a fundamental part of crystalline structures, the remaining polyhedra possess a five-fold rotational symmetry and are thus only found in quasicrystals, since they cannot be used to build a structure featuring long-range order [27].

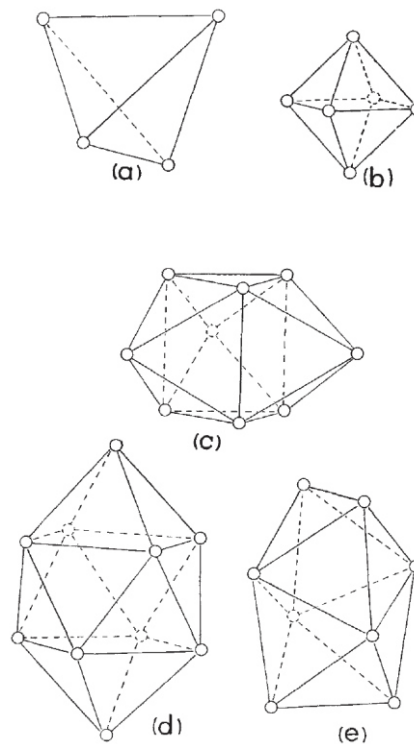


*Figure 4: Five Bernal polyhedra: (a) Tetrahedron, (b) Octahedron; (c) Trigonal prism capped with three half octahedra; (d) Archimedean antiprism capped with two half octahedra; (e) Tetragonal dodecahedron [31].*

### 2.4.1.2. Atomic Distribution Functions

One possibility to qualitatively describe the ordering of MGs, is to measure the deviation from an entirely random ordering of atoms [32]. This can be achieved by conducting a scattering experiment and measuring the scattering intensity and obtaining the scattering structure function  $S(\mathbf{Q})$ . In perfectly isotropic materials such as MGs,  $S(\mathbf{Q})$  is theoretically only

dependent on the magnitude of the Q-vector, representing a radial average in the reciprocal space. It can be used to calculate the pair distribution function (PDF) in the real space, using a Fourier transformation of the scattering intensity. The PDF, also denoted by  $g(r)$ , gives the probability of finding a pair of particles or atoms in the observed volume, which are apart from each other by a certain distance  $r$ . The function  $g(r)$  displays a measure of probability of encountering an atom at a given distance from the reference atom. Another important derived function is the radial distribution function (RDF)  $R(r)$ , which estimates the density, given by the number of atoms, as a function of the distance from a central reference atom located at  $r = 0$ .

$$R(r) = 4\pi r^2 \rho(r) \quad (2)$$

It is thus closely related to the actual structure of the material [33]. In a perfectly random arrangement (without any structural order), the PDF and RDF would have a constant value, not dependent on the distance to the reference atom. With a higher degree of ordering, or oscillations become visible at certain distances from the reference atom. The peak amplitude, as well as the maximum range at which peaks still occur, are a measure for the degree of ordering of an amorphous structure [32]. At sufficiently long distances from the reference atom, the PDF converges to a value of one, indicating the lack of any long-range order (Figure 5).

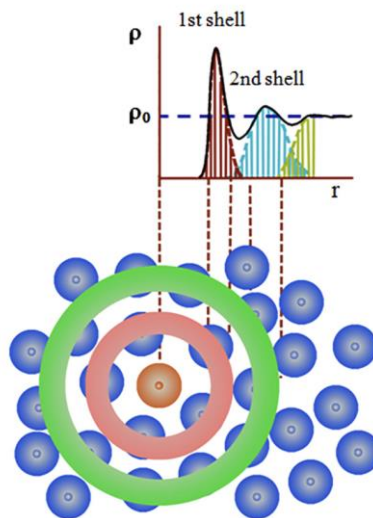


Figure 5: A pair distribution function showing two coordination shells [34].

The oscillations in the PDF can be attributed to coordination shells of neighbouring atoms, which are encapsulating the central reference atom. The first shell represents the nearest neighbours, causing a sharp peak in the PDF, the following shells are less pronounced and converge to a constant value. The maximum radius at which structural information is visible, depends on the degree of ordering [27]. A practical use of the RDF is calculating the number of atomic neighbours of a given shell. An estimate of the number of nearest neighbours of the central atom is the area under the first peak. In order to estimate this coordination number, an integration of the RDF can be performed, the integration range of  $r$  corresponding to the range of the first peak of the RDF:

$$N_c = \int_{r_1}^{r_2} R(r) dr \quad (3)$$

#### 2.4.1.1. Modern Models of the Atomic Structure

Modern atomistic models describing MG structures should give an accurate prediction of several parameters of the material, including density, packing fraction and coordination number. Without a definable repeating unit cell, calculating these values is not trivial for amorphous structures and suitable theoretical approaches need to be used. Another important factor to consider is the effect of different atomic radii in multicomponent alloys. The impact of these values on MG stability and the comparison to close-packed crystal structures is also of interest. Various structural models for estimating density and packing fraction are available, while older models are often refined by recent findings. Numerous models describe the structure of a MG as consisting of atomic clusters. A single cluster is represented by a central atom, surrounded by its first coordination shell, as represented by the first peak in the PDF.

An exemplary model by D. B. Miracle [35] estimates density and packing fraction of binary MGs. In a binary MG, consisting of solute ( $\alpha$ ) and solvent ( $\beta$ ) atoms, a central solute atom is surrounded by solvent sides, forming a cluster. The number of atoms surrounding a central solute atom determines how efficiently the cluster is packed, which also determines if a MG will form. Similarly to how rules found by Hume-Rothery [36] govern the formation of crystalline metallic solid solutions, an equivalent requirement is found in the formation of MGs, which is the efficient filling of space. In the formation of clusters, certain radius ratios  $R$

between the central solute atom and the surrounding solvent atoms will yield an efficient packing. These calculated relative atom radii are present in most of the examined binary MGs, where they form the SRO. The calculated and also observed coordination numbers  $Z$  are 9, 10, 12, 15 and 17, also called cluster packing modes [37].

These packed clusters are themselves efficiently packed, which mostly leads to an arrangement in an face centred cubic (fcc)-type lattice, forming a unique cluster unit cell. The fcc arrangement is only upheld for several cluster diameters, forming the medium-range order (MRO). The interstitial octahedral ( $\beta$ ) and tetrahedral ( $\gamma$ ) sites present in the fcc arrangement can also be occupied by solute atoms if the ratio of atomic radii in binary glasses is suitable (Figure 6).

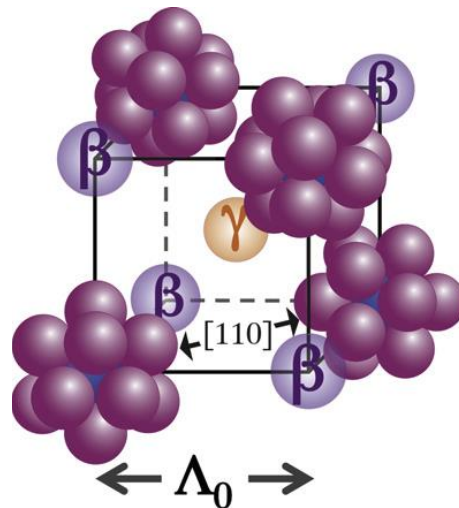


Figure 6: Atomic  $\alpha$ -centered clusters forming a reduced fcc unit cell, with visible octahedral ( $\beta$ ) and tetrahedral ( $\gamma$ ) sites [35].

The chemical composition is an important input parameter for the model, which influences the size of a cluster unit cell and ultimately the density. Estimating the density of a structure is performed by calculating the mass of a single cluster using the radius ratio  $R$ , the solute atom fraction  $f_\alpha$ , as well as the atomic masses. Since a unit cell contains a total of two clusters, the mass of two clusters is then divided by the volume of the reduced unit cell  $(\Lambda_0^{<Z>})^3$  shown in Figure 6, which is also a function of the coordination number  $Z$ . Estimating the length of the reduced unit cell  $\Lambda_0^{<Z>}$  as a function of  $f_\alpha$  and  $R$  is the challenging part of the model. Additionally, the presence of occupied ( $\beta$ ) and ( $\gamma$ ) sites need to be considered.

The obtained model gives a good measure for binary MGs for different coordination numbers  $Z$ , with a mean deviation of  $\Delta\rho = 2.1\%$  between measured and calculated density. Atom packing fractions can be obtained directly from the model and compared against values obtained by using measured density and atomic volumes, also validating the results of this model.

## **2.5. Characterization Methods**

There are numerous analytical techniques used to characterize physical properties of MGs and TFMGs. Typically, nanoindentation is used for measuring hardness, atomic force microscopy (AFM) is applied for gauging surface roughness as well as detecting crystalline phases and dynamic scanning calorimetry (DSC) is used to identify phase transformations and crystallization [4]. Analyses using X-ray diffraction (XRD) and diffraction in a transmission electron microscope (TEM), reveal various aspects of the structure and composition of a TFMG. The focus of this thesis lies on structural characterization of MGs through electron microscopy methods.

### **2.5.1. X-Ray Diffraction Techniques**

#### **2.5.1.1. Laboratory XRD Sources**

A laboratory XRD analysis can be performed to obtain insights onto the general structure of a TFMG and to reveal the occurrence of possible nanocrystalline phases. Entirely amorphous TFMGs do not exhibit any sharp Bragg reflections, as no planes of ordered atoms are present to produce constructive interference of elastically scattered X-rays. In a  $\theta/2\theta$  scan, a broad diffraction peak is indicative of an amorphous phase, while sharp defined peaks originate from a diffraction on distinct crystallographic planes. Nanocrystalline phases which are present in a sufficient amount in an amorphous matrix can be also revealed by XRD analysis [38]. Experiments often involve annealing at higher temperatures to study the crystallization of MGs (Figure 7).



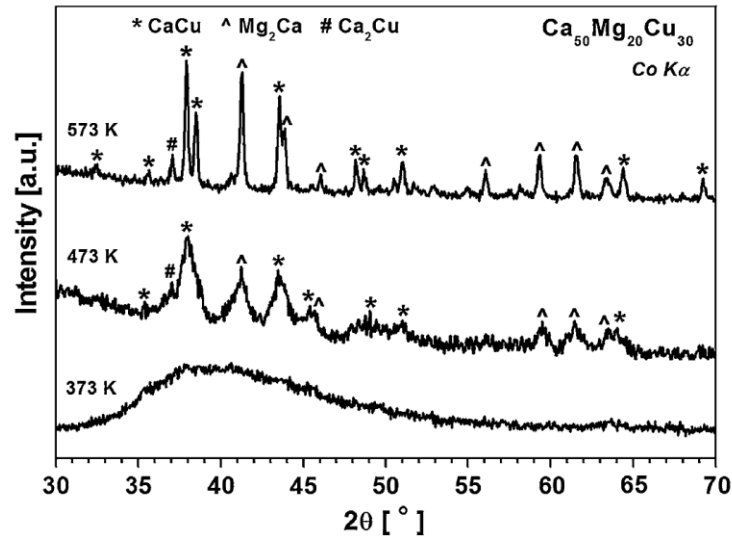


Figure 7: Exemplary XRD pattern of  $\text{Ca}_{50}\text{Mg}_{20}\text{Cu}_{30}$  BMG in as-cast state and subsequently annealed state at higher temperatures. Emerging peaks correspond to three different crystalline phases, growing in size with rising temperature (adapted from [38]).

### 2.5.1.2. Synchrotron X-ray Diffraction

Synchrotron X-ray sources provide higher energy X-rays, which allow for diffraction experiments in transmission Debye-Scherrer geometry, yielding a 2D diffraction image. A possible use-case of in-situ tensile testing enables the observation of elastic behaviour of BMGs. The obtained 2D diffraction pattern can be evaluated through ring segmentation and peak fitting to calculate the strain tensor. Applied tensile load leads to an elliptical diffraction pattern, which can be quantitatively evaluated through the shift in peak position (Figure 8). Through azimuthal integration of the diffraction pattern, the structure factor  $S(Q)$  and in the following the PDF and RDF can be derived, revealing structural information, such as coordination number and nearest-neighbour partials [39].

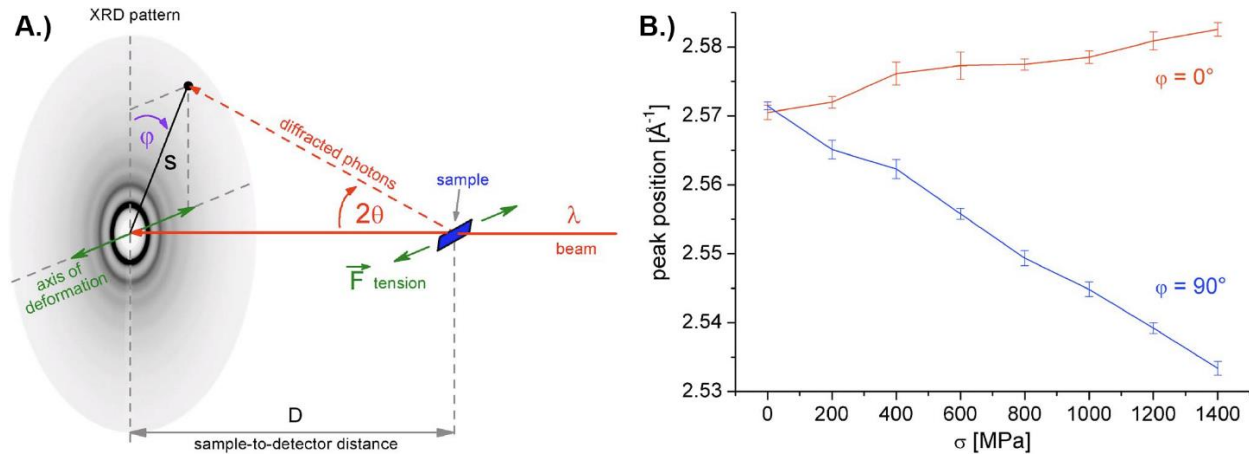


Figure 8: (A) Synchrotron X-ray experiment in transmission geometry producing a circular 2D diffraction pattern in the unstrained state. (B) Shifting of the first fitted peak from the increasingly elliptical 2D diffraction pattern in tensile ( $\varphi = 90^\circ$ ) and transversal direction ( $\varphi = 0^\circ$ ) with tensile loading [39].

### 2.5.2. Conventional TEM Techniques

The TEM benefits from various forms of interaction between electrons and the sample material allowing to gain insight into material structure and composition. The interaction between electrons and the atoms of the sample is stronger than in the case of X-rays. Electrons can be scattered by the atomic nucleus, as well as by the surrounding electron cloud, leading to a higher probability of interaction than using X-rays, which are only scattered by the electron cloud [40]. When performing TEM studies, different operating modes of the TEM are used to extract different types of information about the material.

For TEM investigations the samples need to be sufficiently thin to be electron transparent ( $<100$  nm), requiring dedicated sample preparation techniques. In the case of TFMGs a cross-section specimen needs to be prepared. When using conventional preparation, the thin film is sliced perpendicular to the interface, two slices are glued together to form a sandwich-like structure, which is then mechanically thinned. Ion polishing is used for final thinning. Alternatively, a focused ion beam (FIB) lift-out technique can be used to prepare a TEM lamella. TEM preparation methods may however induce changes to the chemistry and structure of prepared specimens, which can lead to distorted observations and conclusions [41].

### 2.5.2.1. TEM Bright-field, Dark-field and Diffraction Mode

A conventional TEM bright-field (BF) analysis of an unstrained perfect amorphous solid metallic glass sample delivers a featureless micrograph like in Figure 9a. The respective selected area diffraction (SAD) patterns show typical diffuse rings, with a uniform intensity distribution in the azimuthal direction (Figure 9b). The radial intensity distribution reflects the SRO in the material. The diffuse ring observed in diffraction patterns of amorphous materials is often termed “halo”.

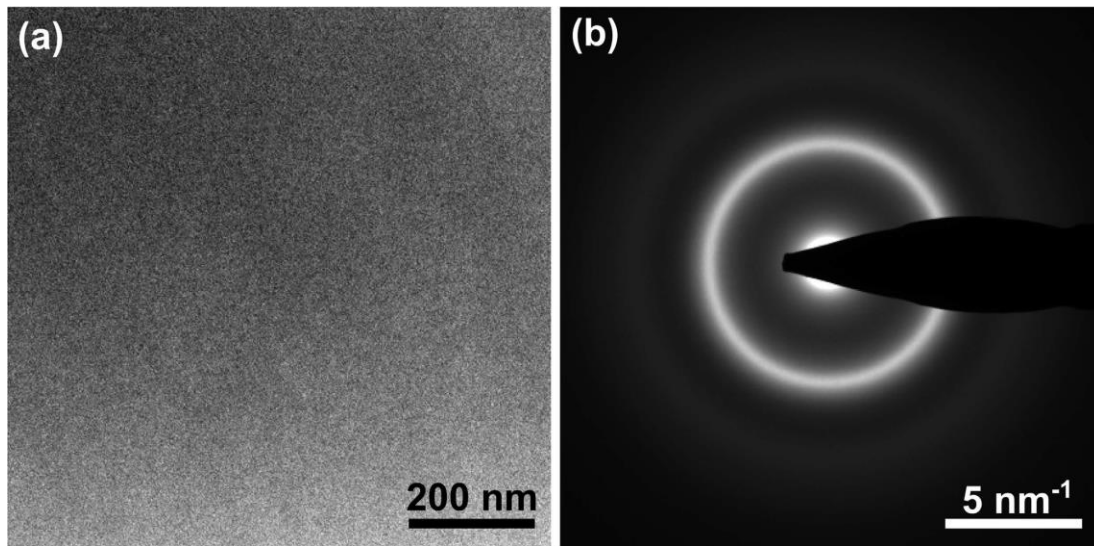
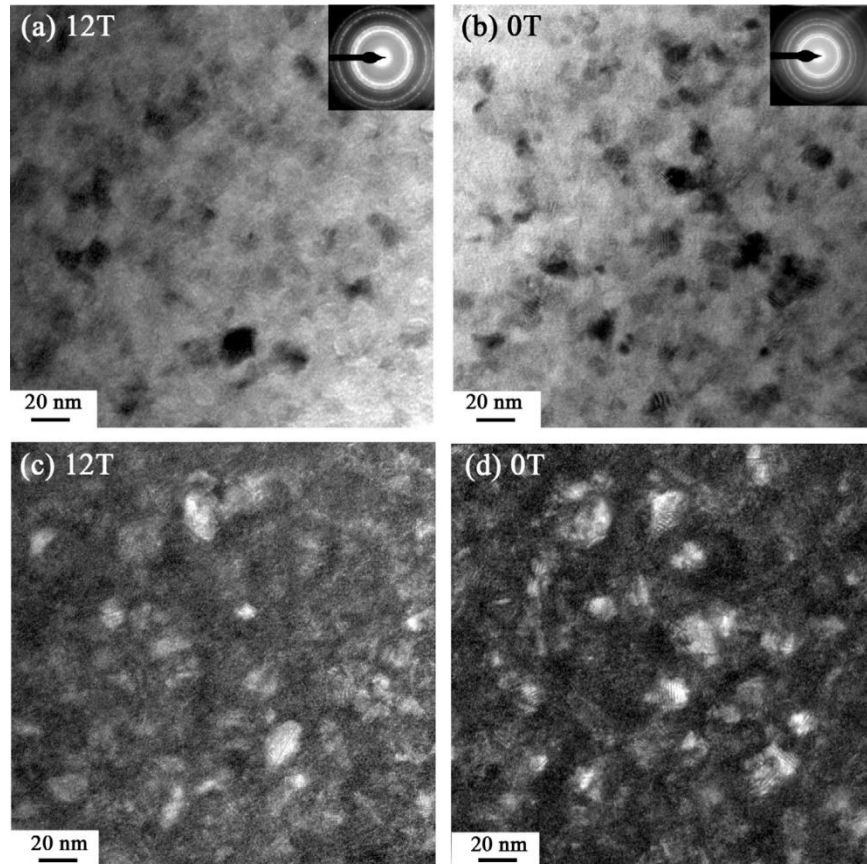


Figure 9: (a) Representative bright-field TEM image of a homogeneous BMG, producing a “halo ring pattern” in SAD (b).

Annealing of the cast BMG sample at temperatures in the region of  $T_x$  can lead to the formation of crystalline phases. In TEM BF mode, a heterogeneous microstructure can be observed, featuring an amorphous matrix and nanocrystalline inclusions, which can be distinguished by contrast (*cf.* Figure 10a, b). The origin and type of contrast in the TEM is dependent on several variables. In TEM BF mode, contrast arises due to mass-thickness contrast and diffraction contrast [40]. Atoms with a higher atomic number  $Z$ , possess a higher scattering cross-section, leading to a stronger scattering of intensities than lighter atoms. Likewise, ordered crystallographic planes in crystalline phases cause stronger scattering of the direct beam, producing higher intensity diffracted beams. They consequently appear darker in the BF image, than the amorphous matrix. The contrary is observable in dark-field (DF) mode (Figure 10c, d), with diffracting nanocrystals appearing brighter than the matrix,

due to higher intensity of the diffracted beams. The presence of crystalline phases always needs to be confirmed by electron diffraction patterns, since darker and brighter regions can also appear in fully amorphous samples, due to mass-thickness contrast variations. SAD patterns visible in the insets of Figure 10a, b feature a broad halo ring caused by the amorphous matrix, together with sharp diffraction rings originating from the nanocrystals [42].



*Figure 10: Exemplary BF (a,b) and DF (c,d) TEM micrographs showing an annealed BMG specimen, featuring an amorphous matrix with nanocrystalline inclusions, as confirmed by diffraction patterns visible in the insets [42].*

### **2.5.2.2. High resolution TEM Mode**

High resolution transmission electron microscopy (HRTEM) is an operating mode which can offer the necessary resolution in order to observe the projected atomic arrangements of materials. Crystalline structures can be imaged by tilting the specimen into zone axis orientation, allowing to image the individual atomic columns. In the case of metallic glasses HRTEM can be used to reveal their amorphous nature, but their atomic arrangement cannot

be directly imaged due to their disordered nature. Such high resolutions require a well aligned microscope. A TEM offering a corrector for spherical aberration ( $C_s$ -corrector), as well as a field emission gun (FEG) allows to obtain higher resolution. The sample region should be thin and flat in order to obtain a micrograph featuring phase contrast [40]. Since the specimen is illuminated by a coherent electron beam, this operating mode is a form of coherent imaging. A disadvantage of the HRTEM method is the dependence on imaging parameters and lens alignment, which can negatively impact the final image. In addition, dynamical diffraction effects, can impact the collected data [43].

### **2.5.3. Scanning Transmission Electron Microscopy**

The fundamental difference of scanning transmission electron microscopy (STEM) to conventional TEM (CTEM), is the formation of the image. In CTEM, the image is formed directly by the electron beam, which passes through the thin sample material and forms an image in the image plane. In STEM mode the beam is condensed to a very small spot, while scanning coils scan the beam over a defined region on the sample. Different detectors can be inserted into the diffraction plane and intensity recorded for each probe position forms the image. This allows the use of multiple characterization techniques. Magnification of the observed image is also controlled differently. In TEM mode, magnification is changed through variation of lens currents, which affects the magnifying power of the lens. In STEM mode, the magnification is solely controlled by the scan dimensions and the step size. The resulting image strongly dependent on the aberrations of the electron probe.

### **2.5.4. Dark-Field STEM**

Detectors such as the annular dark-field (ADF) and high-angle annular dark-field (HAADF) detector record the intensities of scattered electrons. One advantage of dark-field STEM to conventional TEM DF images, is that while in the TEM only a part of scattered electrons can be selected by the objective aperture, the annular STEM detectors collect most of the scattered electrons. Through variation of the camera length  $L$  using imaging lenses, the signal of collected scattered electrons can be maximized on the annular detectors. The ADF detector is recording scattered electrons at angles between  $\approx 0.5^\circ$  than  $\approx 3^\circ$  and thus also include electrons, which are elastically scattered by Bragg diffraction. This contribution can be avoided when using the HAADF detector, as only electrons scattered at angles greater than

$\approx 3^\circ$  are collected, yielding images that feature exclusively  $Z$ -contrast [40]. In comparison to conventional TEM (such as the HRTEM method), STEM imaging is a form of incoherent imaging which is not strongly impacted by imaging parameters and dynamical diffraction effects [43].

### **3. Implementation of the Evaluation Procedure**

#### **3.1. Nanobeam Electron Diffraction in 4D STEM**

Nanobeam electron diffraction (NBED) is a method used in STEM configuration, capable of determining local elastic strains with a high resolution of about 1 nm. While NBED can also be performed on crystalline TEM samples, in this thesis NBED applied to amorphous specimens will be elucidated. The specimen is scanned by a converged electron beam, while a NBED pattern and high-angle annular dark-field (HAADF) signal is recorded at each probe position. The NBED pattern is consisting of a characteristic diffuse halo ring, while a beam stop usually blocks out the direct electron beam. The HAADF-signal recorded at each scan position yields an image featuring  $Z$ -contrast. During acquisition a HAADF-STEM image is shown, while additionally a full NBED pattern is recorded at each probe scan position. Since a full two-dimensional diffraction pattern is recorded for each probe position of the two-dimensional map, the procedure is termed 4D STEM.

Recording 4D STEM maps during in-situ experiments allows for revealing time-dependent material properties and local strain distributions at the nanoscale. Figure 11 shows schematically an exemplary experimental setup in which a bending-beam is loaded in-situ, while 4D STEM datasets are collected for a further strain analysis.

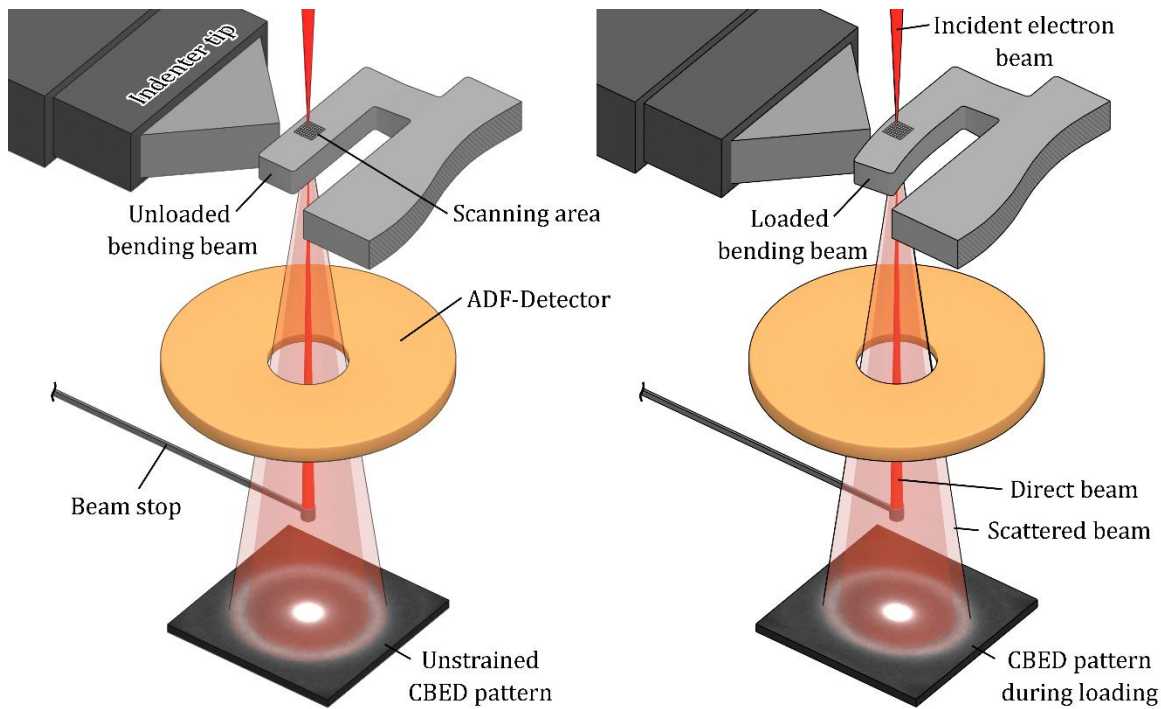
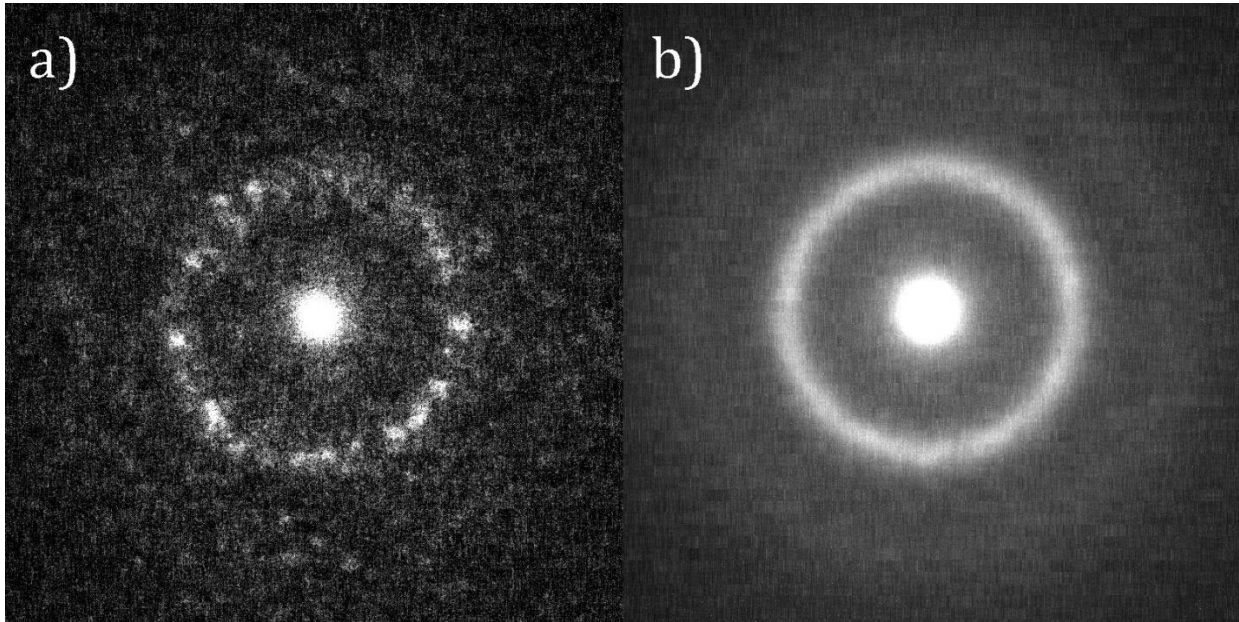


Figure 11: Exemplary experimental setup in the STEM during in-situ loading of an amorphous bending beam. The converged electron beam scans over a defined area, yielding a typical amorphous diffraction ring and a signal from the HAADF detector at each probe position (adapted from [1]).

### 3.1.1. Formation of NBED Patterns

Scanning an amorphous MG TEM specimen with a rather parallel electron nanobeam can yield an image as shown in Figure 12a on the electron detector. The maximal intensity is located in the centre of the image at  $k = 0$ , showing the direct, unscattered beam. A beam stop can be used to prevent damage to the electron detector. At higher radii, a speckled intensity distribution is visible in a certain range  $\Delta k$ . This fluctuating ring-shaped intensity distribution is directly related to the atomic arrangement inside the irradiated volume of the MG sample. With a beam spot-size of around 1.5 nm, the number of atoms which interact with the beam and cause scattering is limited. Only several atomic clusters in the amorphous structure are irradiated at a given beam position, yielding a NBED image which is related to the MRO in the material.



*Figure 12: (a) A typical NBED pattern of an amorphous MG TEM specimen, recorded using a rather parallel beam in STEM mode, with a spot size of around 1 nm. (b) An average diffraction pattern obtained by averaging over 1000 individual NBED patterns showing homogeneous azimuthal intensity distribution.*

Averaging over a sufficient number of diffraction pattern recorded in a certain scan shows a diffuse halo-ring, without intensity fluctuations in the azimuthal direction (Figure 12b). Such a diffraction pattern can also be obtained by using SAD on a purely amorphous sample, as seen in Figure 9b.

### **3.1.2. Effect of Precession Electron Diffraction**

Precession electron diffraction (PED) is a technique which can be used when collecting electron diffraction data from both crystalline and amorphous samples. In a PED setup, the electron beam is not passing through the specimen perpendicularly to the sample surface plane but rather is tilted and performs a rotation around the central axis of the TEM column. This precession is carefully adjusted and offers advantages in the obtained NBED data. In the present work, the aim of the technique is to combine diffraction signal from different tilts, while maintaining a high spatial resolution. This results in a diffraction pattern with a more uniform intensity distribution (*cf.* Figure 13). Obtained data using PED show improved results after the fitting procedure, as will be shown in the conducted parameter study. A critical value is the precession angle, which can vary from  $0^\circ$  (no precession) up to  $1.5^\circ$ .



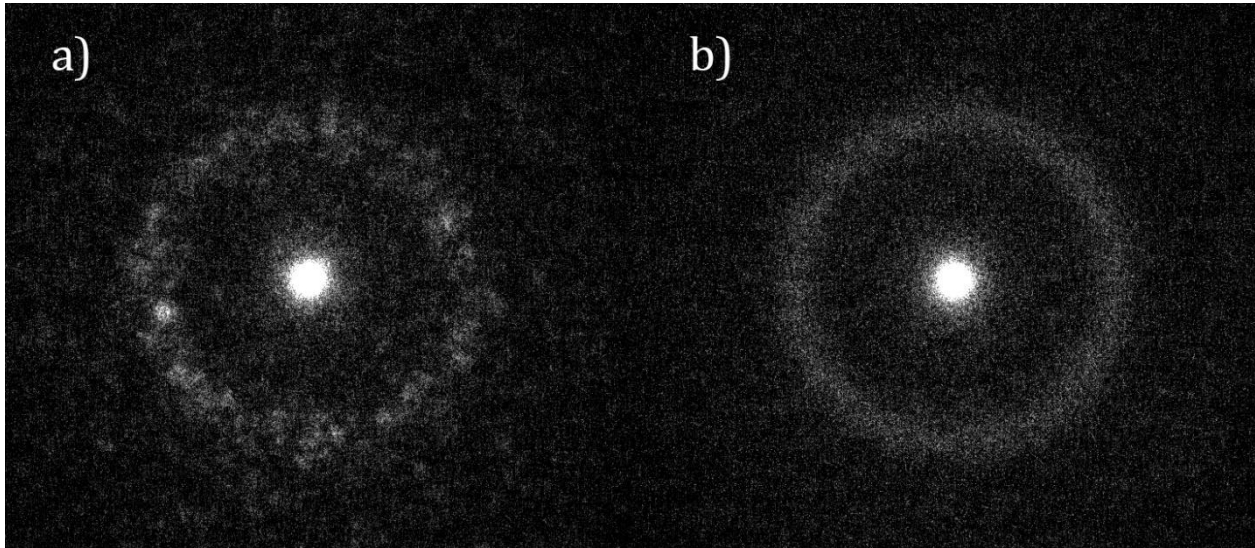


Figure 13: Comparison of exemplary NBED patterns obtained with different scanning parameters, (a) without beam precession, (b) using  $0.5^\circ$  precession.

### 3.1.3. Recording of 4D STEM Maps

As stated before, during the recording of a 4D STEM map, a full NBED pattern is collected at each probe position, together with the signal from the HAADF-detector, which ideally records the amount of inelastically scattered electrons. The main parameters for generating a STEM map are the  $X$ - and  $Y$ -dimensions which lie in the sample plane, the step size between each scan position and the exposure time for a single NBED pattern. A typical set of measurement parameters would be a scan pattern resolution of  $100 \times 100$ , a step size of 2 nm and an exposure time of 100 ms. Another parameter is the resolution of the obtained NBED patterns. The current maximum possible resolution is  $4096 \times 4096$  pixels (px), which however brings several disadvantages, such as the large and quadratically increasing amount of data to store and to process, with an unproportioned profit in precision. Single frame resolutions of  $1024 \times 1024$  px and  $512 \times 512$  px proved to contain all necessary information with sufficient precision, while being easier to record, store and faster to evaluate.

Important microscope parameters are accelerating voltage, spot size, and used aperture, as well as the condenser lens current. The 4D STEM maps in this thesis were recorded on a JEOL JEM-2200FS electron microscope, featuring a field emission gun (FEG) electron source with up to 200 kV accelerating voltage. During scanning, the resulting NBED patterns are recorded on a CMOS camera, featuring a fast acquisition and readout speed. Electron beam precession

and scanning is handled by a TVIPS universal scan generator, which controls the TEM deflection coils. The scan generator is synchronized to the camera system for coordinated recording of NBED patterns. All NBED patterns are stored in a TVIPS file.

### 3.2. Information Contained in NBED Patterns

A single NBED frame contains various parameters of interest which can be obtained through subsequent evaluation. All of the parameters illustrated in the next chapters can be quantitatively evaluated by fitting a parametric two-dimensional ellipse equation to the NBED pattern.

#### 3.2.1. Ring Ellipticity

Considering the evaluation of local atomic strains, the ellipticity of the so-called “diffuse halo ring pattern” is of primary interest. The ellipticity can be defined as a change in the position of the radial intensity maximum, with the azimuthal angle  $\delta$  of the ring (Figure 14). This corresponds to a directional change in interatomic distances in the irradiated volume. Elastic strains change interatomic distances along a specific direction, which causes ellipticity in the amorphous ring pattern. A change of the maximal intensity position to smaller  $k$  values in  $x$ -direction (Figure 14a), indicates an expansion of interatomic distances in this direction and vice-versa (Figure 14b). With this information, the elastic strains  $\varepsilon_{xx}$ ,  $\varepsilon_{xy}$  and  $\varepsilon_{yy}$  in the sample plane can be evaluated from the ring ellipticity [1].

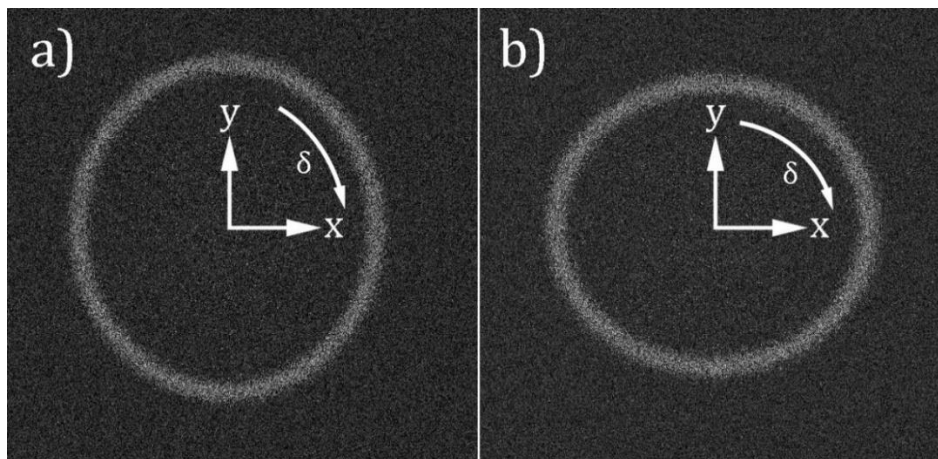
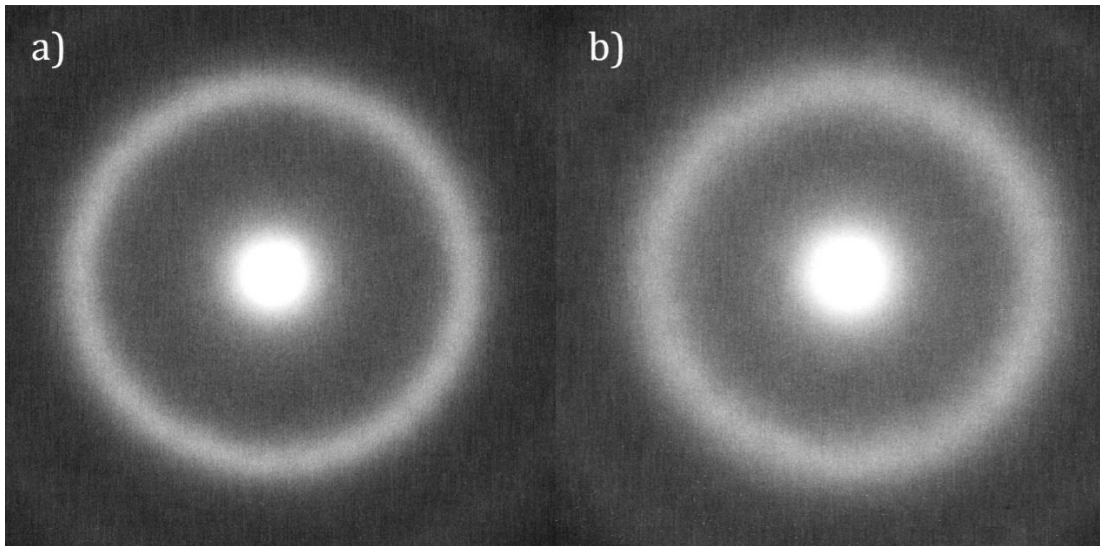


Figure 14: Artificially generated NBED diffraction patterns showing exaggerated ellipticity in the  $y$ - (a) and  $x$ - (b) direction respectively.  $\delta$  indicates the azimuthal angle.

### 3.2.2. Mean Ring Radius and Width

In addition to the ellipticity, the diffuse halo ring can also show a varying mean radius at different probe positions. The ring radius corresponds to the mean interatomic distance in the irradiated volume. A smaller value of the ring radius indicates a larger interatomic distance in the SRO of the irradiated volume. The scattering intensity can be calculated from the azimuthally integrated ring pattern, from which the RDF can be calculated.

Similarly, the width of the diffuse halo ring gives information about the distribution of atoms in the SRO of the material. A sharp halo ring featuring a small width, correlates to nearest neighbour distances which are not greatly deviating from their collective mean bond length. Halo rings showing a larger width, indicate that the values of nearest neighbour distances of individual atoms in the SRO are more widely distributed. The radius and width of the halo ring thus reveal structural information about the observed material (Figure 15).



*Figure 15: Averaged NBED patterns of two different phases (a, b) showing diffuse halo rings with a variation in ring width.*

### 3.2.3. Ring and Background Intensity

Each NBED pattern can be azimuthally integrated to obtain the scattering intensity distribution. A Fourier transformation of this scattering intensity yields the atomic distribution function of the probed volume. The first maximum of the atomic distribution function correlates to the intensity maximum of the diffuse halo ring. The intensity of

the diffuse halo ring has multiple dependencies, such as the elastic scattering cross section, which is a function of the atomic number  $Z$  [40], but also the degree of ordering. Regions with high  $Z$  show a higher maximal intensity ring, than regions with a low  $Z$ . The amount of elastic scattering however, also increases with increasing sample size, although it can be obscured by inelastically scattered electrons in microscopes without an energy filter.

Intensity and slope of the background are also parameters which can be extracted from NBED patterns. These are as well related to the composition of the observed volume and the sample thickness.

### 3.3. Evaluation of NBED Patterns

Gaining insight into local atomic strains, as well as structure and composition of observed amorphous materials, requires a suitable evaluation method of obtained 4D STEM diffraction maps. Most frequently, NBED patterns featuring amorphous rings are evaluated by segmentation and subsequent individual azimuthal integration, enabling evaluation of local atomic strains.

#### 3.3.1. Parametric Ellipse Equation

In this thesis, an alternative approach will be shown, featuring a two-dimensional fit of a parametric ellipse equation to obtained diffraction patterns. This allows evaluation of local atomic strains, as well as providing information about material structure and composition. The equation to be fitted to the recorded data is as follows:

$$e(x, y) = p_4 * \exp \left[ - \frac{(r_0 - \sqrt{p_0(x - x_0)^2 + p_1(x - x_0)(y - y_0) + p_2(y - y_0)^2})^2}{2p_3^2} \right] + p_5 + p_6 \sqrt{(x - x_0)^2 + (y - y_0)^2} \quad (4)$$

A 3D representation of this function in Figure 16 illustrates its relation to obtained NBED patterns from amorphous samples in Figure 12.

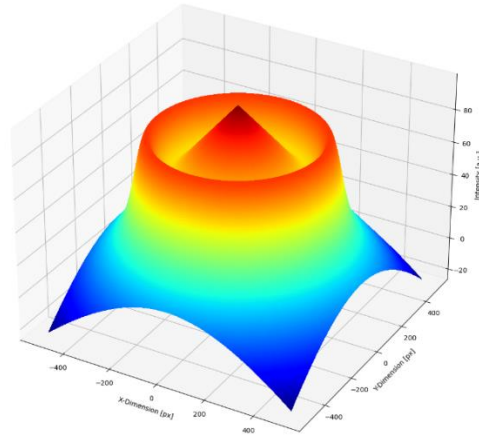


Figure 16: A 3D surface plot of the parametric ellipse equation (4) using parameters from a fitted dataset.

The occurring nine independent parameters in equation (4), each describe a certain shape aspect of the ellipse, as well as its background and shift. All nine fitting parameters are varied to approximate the function to the diffraction patterns. A brief description of the effect of changing each fitting parameter independently is provided below.

The parameters  $p_0$ ,  $p_1$ , and  $p_2$  from equation (4) predefine the ellipticity of the function, each one in a different dimension, as discernible in Figure 17. Strain values can be calculated from these parameters, to form the two-dimensional strain tensor. The practice of performing 4D STEM scans and obtaining strain values for each probe position is termed strain mapping.

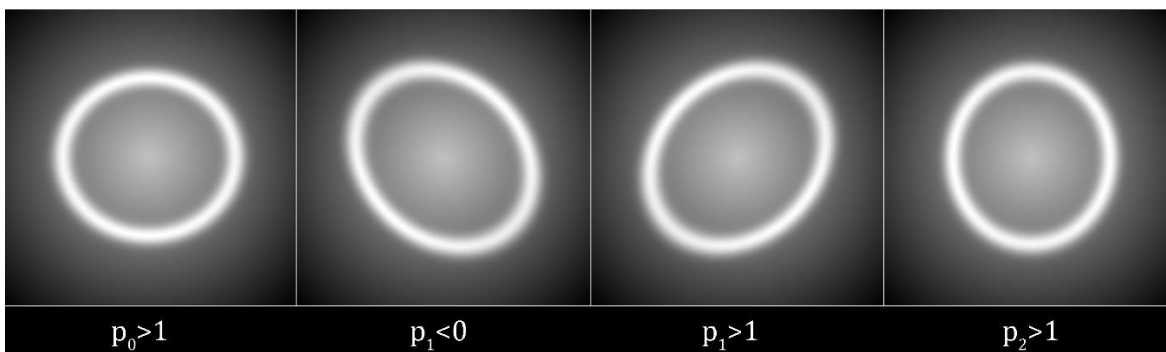


Figure 17: The effect of fitting parameters  $p_0$ ,  $p_1$ , and  $p_2$  on the ellipticity of the parametric function, (axis scaling is arbitrary).

Parameter  $p_3$  controls the width of the ellipse ring, while  $p_4$  controls the maximum intensity of the ellipse. The background parameter  $p_5$  adds a constant value to each point of the function and thus creates a shift in intensity of the whole function. Parameter  $p_6$  indicates the

slope of the background, which can be either concave or convex. Usually, the diffraction patterns show a convex background profile, equivalent to a two-dimensional gaussian peak.

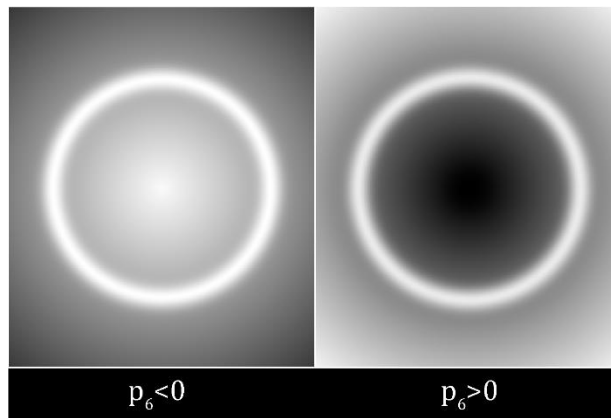


Figure 18: Effect of the fitting parameter  $p_6$  on the background profile of the parametric function.

The parameters  $x_0$  and  $y_0$  specify the shift of the function in the  $xy$ -plane. For a perfectly centered function, both values are zero. The centring of diffraction patterns in the pre-processing procedure is however not perfect, thus the shift of the function is included as a fitting parameter.

### 3.3.2. Technical Implementation of 4D STEM-Map Strain Evaluation

With the aim of a fast and precise strain evaluation through multidimensional fitting, a Python software package was created. The use of various libraries facilitates fast treatment of a large number of NBED patterns. Furthermore, the entire evaluation procedure can be controlled using a graphical user interface (GUI), displaying the current frame, next to the fitted result (Figure 19). The GUI is designed using the *PyQt5* library, which provides an easy access to the *Qt* GUI framework in Python. Important used libraries are the *NumPy* [44] library for calculations, *SciPy* [45] for the fitting of parametric equations to two-dimensional data, and *PIL* [46] for various operations on data in image format. In addition, the *Ray* framework was used for implementing a fit procedure, that can be distributed across multiple CPU cores, greatly improving processing time and scalability. In the following

paragraphs, a regular data evaluation procedure will be elucidated from raw data to visualization of results.

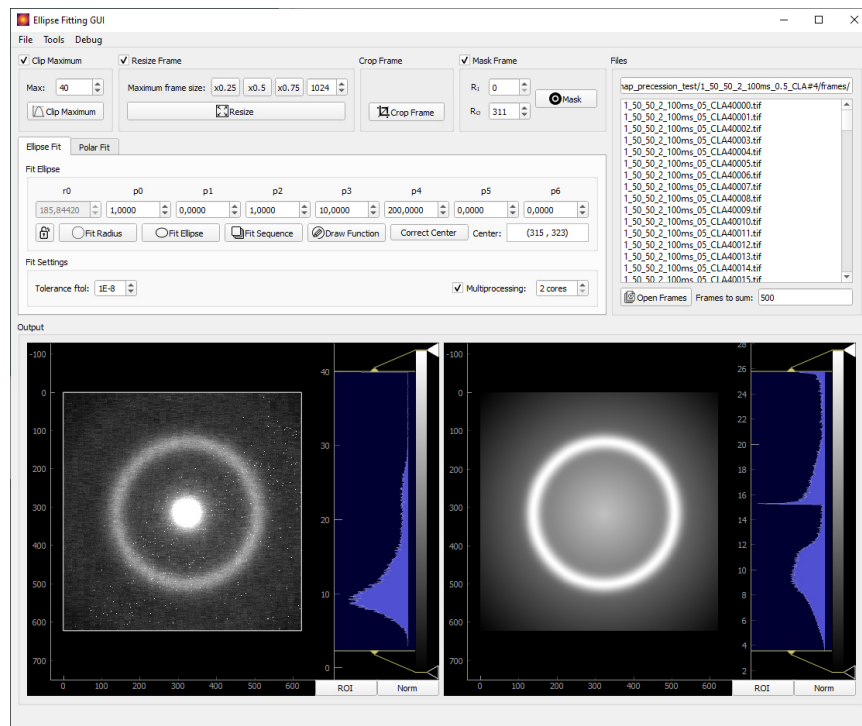


Figure 19: The main GUI window controlling file handling and fitting.

### 3.3.3. Data Conversion and Frame Alignment

The first step is a necessary conversion of the recorded TVIPS files into a filetype that is easier to handle. For this purpose, the TVIPS files are opened and converted into the hierarchical data format HDF5, from which the separate diffraction patterns are extracted as TIFF files. During this conversion, a required beam centre correction is performed since the beam centre is usually slightly shifting during scanning. Two approaches were tested for speed and precision, both using cross-correlation. Cross-correlation compares two signals regarding its similarity and shift. The first approach involves mirroring each frame along the x and y axis and performing a cross-correlation with the un-mirrored frame. Another possibility is to select only the direct unscattered beam as a region of interest (ROI) and cross-correlate this with the current frame. The latter method proved to be faster and more precise, showing the beam shift in x and y direction as a function of the frame number. As the scan measurement of one row is finished and the beam shifts to the next row, a reversal of the shift direction is

clearly visible in the correction data (Figure 20). However, this method does not work, if the direct beam is obscured by a beam-stop.

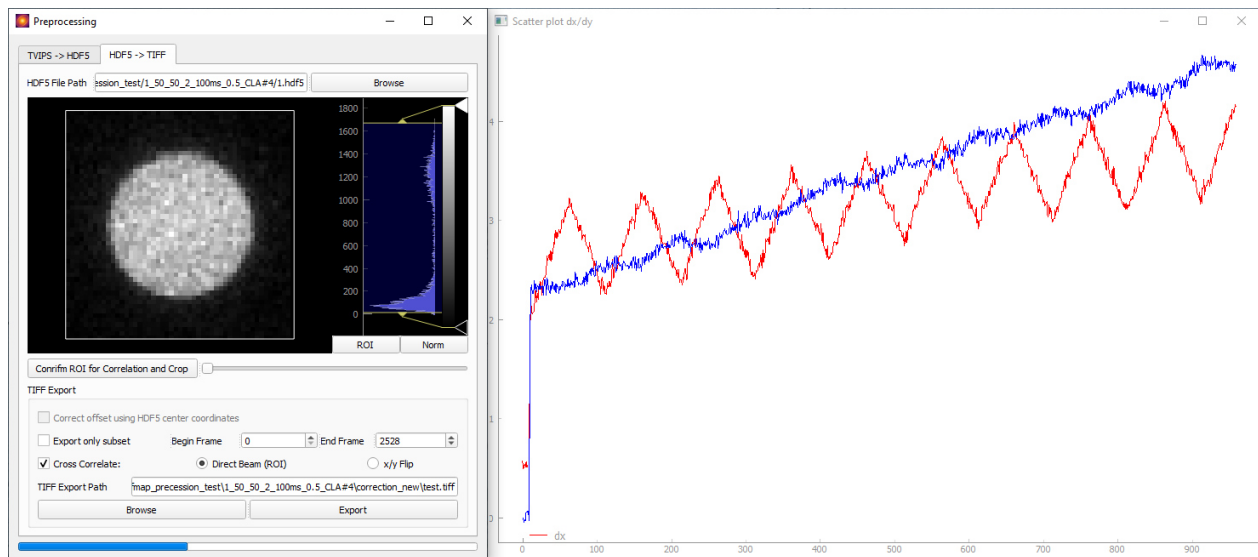


Figure 20: The beam centre correction using the direct beam as the ROI (left) and performing cross correlation on each frame. Results of the cross correlation clearly show the oscillating beam shift in horizontal ( $x$ ) direction during scanning (right, red line), as well as the vertical shift ( $y$ , blue line).

### 3.3.4. Frame Pre-processing Steps

At this point, all NBED patterns are present as centred TIFF files, which is necessary for the fitting procedure. Before fitting the 4D STEM map however, parameters for certain data pre-processing steps need to be set. First, an average frame is generated by selecting a subset of around 100 frames from the total scan. The following calculations are then carried out on the average frame, to show its effect and are afterwards applied to each frame before the fitting procedure.

Truncating the maximum intensity of each NBED frame at a specific value is required. Otherwise, the high intensity of the direct beam, which usually greatly exceeds that of the diffuse halo ring, would hinder an efficient fit. The value for truncating is selected manually in a way that allows the diffuse halo ring to fill a large part of the intensity histogram. Additionally, the intensity distribution of the frame is normalized to an intensity range with its minimum value at zero.

The next step is optional and involves resizing the frames, which can be performed either by multiplying the frame pixel size with a float value or specifying a resolution, to reduce



processing time. With the aim of excluding unnecessary data from the fitting procedure, the frame can also be additionally cropped, which is performed by manually selecting a ROI in the GUI.

After these steps, a modification of the parametric ellipse equation is fitted to the averaged frame. The equation describes a circle, which is as follows:

$$e(x, y) = p_4 * \exp \left[ -\frac{(r_0 - \sqrt{(x - x_0)^2 + (y - y_0)^2})^2}{2p_3^2} \right] + p_5 + p_6 \sqrt{(x - x_0)^2 + (y - y_0)^2} \quad (5)$$

Fitting the circle to the averaged diffuse halo ring allows determination of its exact centre, which is necessary for the next step. Additionally, the radius of the fitted circle  $r_0$  is an important metric for the subsequent interpretation of fitted data. If using an averaged frame, consisting of sufficient singular frames for fitting, the fitted circle with radius  $r_0$  should give a reasonable estimate of a diffraction patterns of a locally unstrained material.

After the exact centre has been determined, an annular mask can be overlayed over each NBED pattern prior to fitting. This can be performed, if all data except the diffuse halo ring need to be excluded from the fitting procedure, which further improves processing time, but can impact fit precision.

### 3.3.5. Fitting Procedure

The averaged frame now has been treated with some or all of the above processing steps. Prior to fitting the full 4D STEM map, the parametric ellipse equation will be fitted to the averaged and processed frame, to confirm that a successful fit will be possible for the singular frame.

For this purpose, initial fit values for all parameters of the ellipse equation need to be specified. The GUI comes pre-filled with reasonable default values on program start-up, however values closer to the fitted value may improve overall evaluation speed. Finding close to optimal parameters can be performed iteratively: The ellipse can be fitted to the averaged frame using initial parameters, giving fit results and residual fit error (Figure 21). The initial parameters can be tweaked to lie closer to the fit results. Inserting the exact fitted parameters

as initial values however mostly does not deliver an optimal fit, neither in processing time, nor in residual fit error. Once suitable initial values have been found, the whole 4D STEM map can be fitted, which is started with the *Fit Sequence* button.

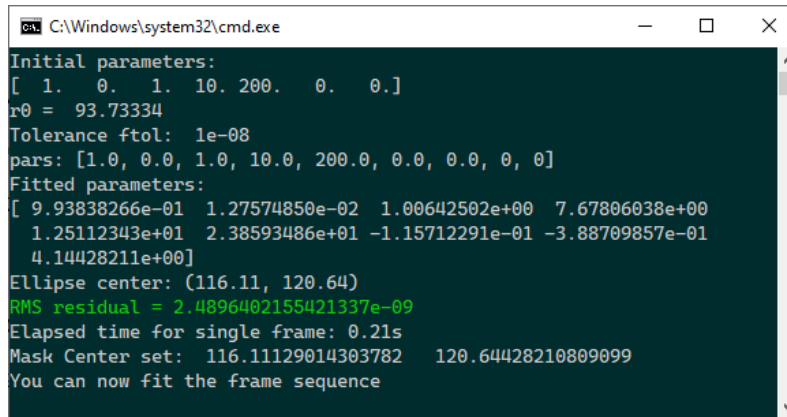
### 3.3.5.1. Programmatic Implementation

The *SciPy* library provides a suitable method of fitting parametric equations such as Eq. 4 to two-dimensional data. Concretely, the `scipy.optimize.curve_fit` function is used, which has the following syntax (unused arguments are excluded):

```
scipy.optimize.curve_fit(f, xdata, ydata, p0, bounds, ftol)
```

The first argument `f` refers to the function to be fitted to the supplied data, which is the parametric ellipse equation Eq. 4. `xdata` is defined as the two-dimensional array of the frame. For an exemplary resolution of 1024x1024, the array has  $1024^2$  entries. `ydata` represents the actual intensity distribution of the two-dimensional frame, extracted from the diffraction pattern to be fitted. `p0` is the array of initial parameters, which were set using the GUI. `bounds` is an array containing upper and lower boundaries for the fitting parameters  $p_1$  to  $p_6$ , as well as  $x_0$  and  $y_0$  with the aim of improving fit stability and speed. `ftol` defines the tolerance between fitted function and data, after which further optimization is stopped, the default value being  $10^{-8}$ .

The fitting algorithm uses a non-linear least squares approach. The function parameters are altered with the aim of minimizing the error between the data and the function. After a successful fit, the `curve_fit` function returns the determined optimal parameters of the fitted function, as well as the variance of the parameters. The fit error is calculated as a root mean square (RMS) value from the difference of supplied data and fitted function (Figure 21).



```

C:\Windows\system32\cmd.exe
Initial parameters:
[ 1. 0. 1. 10. 200. 0. 0.]
r0 = 93.73334
Tolerance ftol: 1e-08
pars: [1.0, 0.0, 1.0, 10.0, 200.0, 0.0, 0.0, 0, 0]
Fitted parameters:
[ 9.93838266e-01 1.27574850e-02 1.00642502e+00 7.67806038e+00
 1.25112343e+01 2.38593486e+01 -1.15712291e-01 -3.88709857e-01
 4.14428211e+00]
Ellipse center: (116.11, 120.64)
RMS residual = 2.4896402155421337e-09
Elapsed time for single frame: 0.21s
Mask Center set: 116.11129014303782 120.64428210809099
You can now fit the frame sequence

```

Figure 21: Command-line output after fitting a single diffraction pattern, containing initial parameters fitted parameters, RMS residual and elapsed time.

### 3.3.5.2. Multiprocessing Implementation

The described fitting procedure normally only runs on a single CPU core, which causes long processing times for large 4D STEM maps. However, Python offers multiple possibilities of parallelizing computationally demanding tasks, which can greatly decrease processing times. After testing different solutions, the *Ray* framework was selected to distribute the fitting procedure asynchronously to multiple CPU cores. Implementing this multiprocessing approach involves starting a number of independent processes for fitting, one for every CPU core. After initialization of the *Ray* framework, each process receives a single diffraction pattern for fitting, together with initial parameters and its position in the 4D STEM map. Each process then outputs the fitted parameters and RMS residual (Figure 22). Since the asynchronously working processes finish fitting with different computing times, the fit results need to be sorted by frame number at the end of the whole procedure.

Another possibility of parallelization is offloading the computation to a performant graphics processing unit (GPU), since its architecture is suited for calculating problems of this type. When using the Python *pygpufit* library together with the *CUDA*-enabled GPU, the parametric ellipse equation needs to be defined in C++ as a custom fitting function. At this time, a successful fit was not achievable.

```

C:\Windows\system32\cmd.exe
Fitting a total of 2500 frames with 6 CPU processes.
2022-01-23 16:21:09,621 INFO services.py:1171 -- View the Ray dashboard at http://127
.0.0.1:8265
.....
Parameters: {'ROI_size': Point(233.282109, 233.282109), 'ROI_position': Point(144.34
1280, 144.646546), 'clip': True, 'clipval': 50, 'resize': True, 'resizeval': 0.5, 'ma
sk': False, 'mask_center': (0, 0), 'mask_ri': 0, 'mask_ro': 0, 'ftol': 1e-08}
(pid=18036) Program variables initialized!
(pid=30128) Program variables initialized!
(pid=21012) Program variables initialized!
(pid=14988) Program variables initialized!
(pid=25204) Program variables initialized!
(pid=26348) Program variables initialized!
(pid=26348) Frame 1_50_50_2_100ms_05_CLA40000.tif: RMS = 1.60305e-08 time = 0.4
(pid=18036) Frame 1_50_50_2_100ms_05_CLA40004.tif: RMS = 6.16783e-09 time = 0.429
(pid=30128) Frame 1_50_50_2_100ms_05_CLA40005.tif: RMS = 2.17371e-08 time = 0.431
(pid=21012) Frame 1_50_50_2_100ms_05_CLA40002.tif: RMS = 3.58656e-08 time = 0.428
(pid=14988) Frame 1_50_50_2_100ms_05_CLA40001.tif: RMS = 8.50053e-09 time = 0.408
(pid=25204) Frame 1_50_50_2_100ms_05_CLA40003.tif: RMS = 4.08082e-08 time = 0.408
(pid=30128) Frame 1_50_50_2_100ms_05_CLA40010.tif: RMS = 3.77222e-08 time = 0.398
(pid=21012) Frame 1_50_50_2_100ms_05_CLA40009.tif: RMS = 2.27005e-08 time = 0.42
(pid=14988) Frame 1_50_50_2_100ms_05_CLA40008.tif: RMS = 5.99929e-09 time = 0.416
(pid=25204) Frame 1_50_50_2_100ms_05_CLA40007.tif: RMS = 5.85884e-09 time = 0.426
(pid=26348) Frame 1_50_50_2_100ms_05_CLA40006.tif: RMS = 6.40439e-08 time = 0.386
(pid=18036) Frame 1_50_50_2_100ms_05_CLA40011.tif: RMS = 3.51683e-08 time = 0.421
(pid=14988) Frame 1_50_50_2_100ms_05_CLA40013.tif: RMS = 9.17297e-09 time = 0.37
(pid=26348) Frame 1_50_50_2_100ms_05_CLA40012.tif: RMS = 2.63179e-08 time = 0.405

```

Figure 22: Command-line output at the beginning of a multiprocessing procedure containing passed parameters and the RMS residual of each frame. The order or frame numbers reveals the asynchronous nature of the procedure.

### 3.3.6. Visualization of Fitting Results

After evaluating a full 4D STEM map, the fitted parameters are available in a CSV file as a list sorted by frame number. Measurements are usually visualized as heatmaps, in which a selected fitted parameter, or an expression containing multiple parameters is plotted as a function of  $x$  and  $y$  coordinates. The coordinate axes are identical to the scanning dimensions of the 4D STEM map.

Heatmaps can be generated in a multitude of plotting programs. With the aim of a simple and straightforward possibility of viewing the results after fitting, a plotting tool was programmed in Python. Figure 23 shows the GUI of this tool, together with an exemplary heatmap of a fitted parameter for a multi-layered sample. After importing a CSV file, the mesh dimensions of the 4D STEM map need to be specified, after which a fitted parameter can be selected for plotting. The tool also allows plotting custom expressions consisting of multiple parameters.

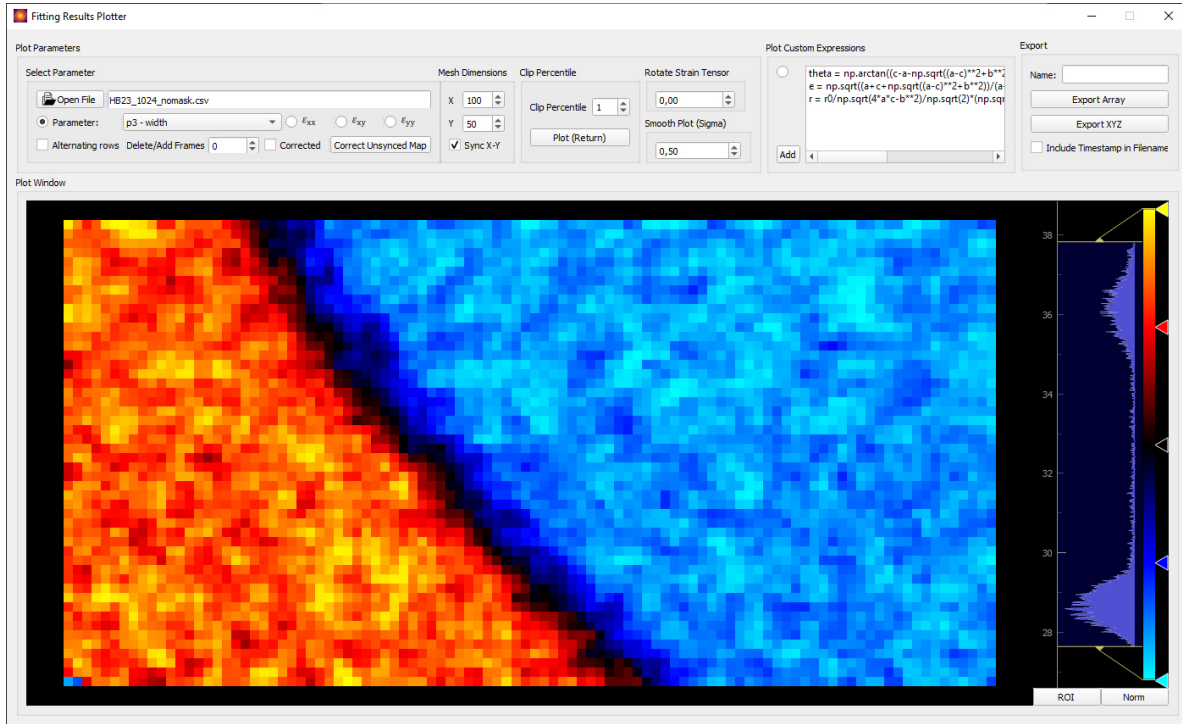


Figure 23: The GUI of the plotting tool, with an exemplary generated heatmap of an interface of a multi-layered sample. The heatmap shows the  $p_3$  ellipse width parameter as a function of  $x$  and  $y$  dimension.

After plotting, the heatmap can be saved as an image, or exported as a CSV file, containing only the selected parameter.

### 3.3.6.1. Calculation of Strains

Plotting the in-plane strains  $\varepsilon_{xx}$ ,  $\varepsilon_{xy}$  and  $\varepsilon_{yy}$ , calculated from the fitted ellipticity parameters is also possible. The two-dimensional plane strain tensor can be calculated from the fitting parameters  $p_0$ ,  $p_1$ , and  $p_2$ , which describe the ellipticity of the fitted parametric function. The strain values are obtained using the following conversion [1]:

$$\varepsilon_{xx} \approx \frac{1}{2}(p_0 - 1) \quad \varepsilon_{xy} \approx \frac{1}{2}p_1 \quad \varepsilon_{yy} \approx \frac{1}{2}(p_2 - 1) \quad (6)$$

Calculating all three strain values for every fitted frame, yields the two-dimensional strain tensor (Eq. 7) for every probe position.

$$\boldsymbol{\varepsilon}_{ij} = \begin{bmatrix} \varepsilon_{xx} & \varepsilon_{xy} \\ \varepsilon_{yx} & \varepsilon_{yy} \end{bmatrix} \quad (7)$$

In this case the  $x$ - and  $y$ -directions correspond to the axes of the diffraction pattern. If strains in other directions than the laboratory coordinate system (such as principal normal strains) are of interest, the calculated strain tensor can be rotated by a specific angle  $\theta$ , using Eq. 8. The heatmap of a component of the rotated strain tensor is then directly plotted.

$$\begin{aligned}
 \varepsilon_{xx'} &= \varepsilon_{xx} \cos^2\theta + \varepsilon_{yy} \sin^2\theta + 2\varepsilon_{xy} \sin\theta \cos\theta \\
 \varepsilon_{yy'} &= \varepsilon_{xx} \sin^2\theta + \varepsilon_{yy} \cos^2\theta + 2\varepsilon_{xy} \sin\theta \cos\theta \\
 \varepsilon_{x'y'} &= (\varepsilon_{yy} - \varepsilon_{xx})\sin\theta \cos\theta + \varepsilon_{xy}(\cos^2\theta - \sin^2\theta)
 \end{aligned} \tag{8}$$

### 3.3.7. Virtual BF and DF

Acquired 4D STEM maps containing all NBED images can be used to obtain virtual images by introducing a virtual aperture to select a specific region in the diffraction patterns. When performing a nanobeam scattering experiment on amorphous materials, the diffraction patterns contain the direct beam, as well as the scattered diffuse halo ring. To form a virtual BF (VBF) image, the direct beam is selected in the NBED pattern using a circular ROI, which is analogous to introducing a virtual aperture. The intensity inside the ROI is then averaged to obtain one value for every NBED pattern in the 4D STEM map. This value is then mapped to show a VBF image with the scanning dimensions of the 4D STEM map, in which each pixel corresponds to one averaged value of a single NBED pattern. Similarly, scattered intensities can be selected by a selection of arbitrary shape, to form virtual DF (VDF) images.

## 4. 4D STEM Parameter Study

### 4.1. Experiment

In this study, five different diffraction strain mapping measurements were conducted consecutively by applying five sets of scanning parameters. The aim was to evaluate the impact of scanning parameters on the quality of the collected data, as well as the importance of fitting parameters and its impact on obtained results.

All experiments were performed on the identical unstrained sample, which consisted of a Cu–Zr–Al BMG. The material was selected due to its frequent use as a model system for experiments and simulations in the field of BMG. It consists of low-cost elements and can be solidified in larger geometries thanks to its good GFA. The BMG system also features good mechanical properties, making it attractive for technological applications. A bulk Cu–Zr–Al BMG was used to prepare a TEM lamella using a focused ion beam (FIB) lift-out technique. For this purpose, a Zeiss AURIGA CrossBeam workstation was used, with a final TEM lamella thickness of  $\sim 100\text{nm}$ .

The investigated scanning parameters are primarily beam precession angle, exposure time, and condenser lens (CL) aperture. The scanning parameters are summarized in Table 1.

*Table 1: Scanning parameter sets used for five strain measurements. The parameter that was changed is highlighted.*

Measurement	Scan rows	Scan columns	Step size (nm)	Exposure time (ms)	Precession Angle (deg)	CL Aperture
1	50	50	2.4	100	0.5	CLA #4
2	50	50	2.4	50	0.5	CLA #4
3	50	50	2.4	100	0	CLA #4
4	50	50	2.4	100	0.5	CLA #3
5	50	50	2.4	100	1	CLA #4

## 4.2. Evaluation

Each measurement yielded 2500 NBED patterns, each with a dimension of 1024 x 1024 px, which were directly fitted using the parametric ellipse equation (Eq. 4). In addition to assessing the individual influence of the scanning parameter sets (Table 1) the second part of this study analyses how different fitting parameters (*i.e.*, settings) influence the final fitted parameters and their standard deviations (Table 2). Therefore, frames of all five measurements were evaluated repeatedly, while the following fitting parameters were varied:

- A radial mask to only fit the ring pattern and mask the direct beam.
- Resize factor (binning) of the frame to obtain a lower resolution prior to fitting.
- The tolerance  $ftol$  for the residual error of the fit: Lower values force a higher number of fit iterations, until the desired tolerance is met, or the maximum number of iterations is reached.

Varying these parameters could potentially retain the fit accuracy, while simultaneously decreasing the computational workload, or also accelerate the fit procedure, while potentially corrupting the fit accuracy. Fitting the full, unresized diffraction pattern with a low RMS tolerance, is expected to deliver the highest fit accuracy, however with higher processing times. To investigate this, the fit parameter combinations from the Table 2 were applied.

Table 2: Used fitting parameter sets and fit convergence criteria.

Mask	Resize factor	RMS Tolerance	Fit designation
No	1	1E-14	Full 1E-14
No	1	1E-8	Full 1E-8
No	0,5	1E-8	Half 1E-8
Yes (Figure 24b)	1	1E-14	Mask 1E-14
Yes, small (Figure 24a)	1	1E-14	Mask small 1E-14
Yes (Figure 24b)	0,5	1E-8	Mask Half 1E-8

One tested method to improve the fit speed and accuracy was based on the application of the masked frames (Table 2). The measured frames were subjected to a pre-processing step, in which the frame was overlaid with an annular mask, omitting certain data points from the



fit. Masks can have different sizes (Figure 24): a larger mask increases fitting speed, while potentially decreasing fit accuracy and vice-versa.

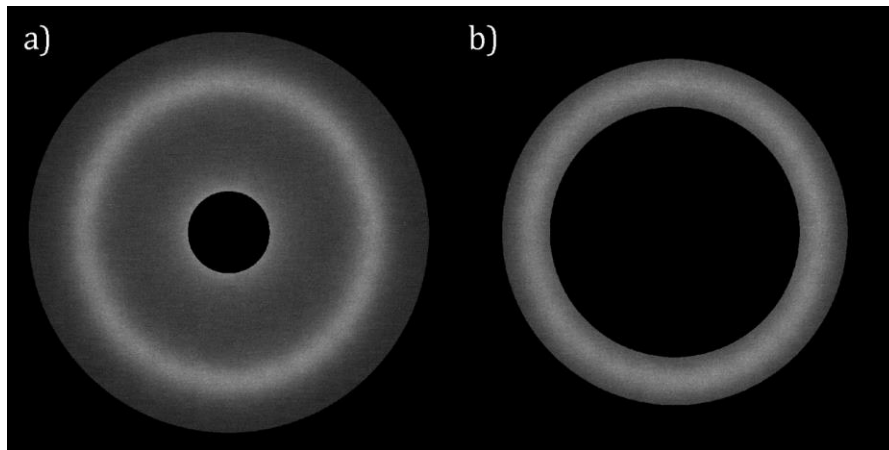


Figure 24: Examples of masked frames: (a) A smaller mask, omitting only the direct beam. (b) A mask only leaving the diffuse halo ring.

### 4.3. Results and Discussion

#### 4.3.1. Discussion of the Influence of Scanning Parameters

The standard deviations of the refined fitted parameters  $p_0$ ,  $p_1$ , and  $p_2$ , which describe the ellipticity of the amorphous ring pattern, are taken as a measure of the accuracy of each measurement. Since the scanning parameters from Table 1 are of primary interest in this section, the influence of parameters (*i.e.*, settings) for fitting needs to be avoided. For this purpose, the standard deviations of fitted results were calculated for every set of different fitting parameters and then averaged. Figure 25 shows the averaged standard deviations of selected fitted results for each measurement (*i.e.*, scanning parameter set).

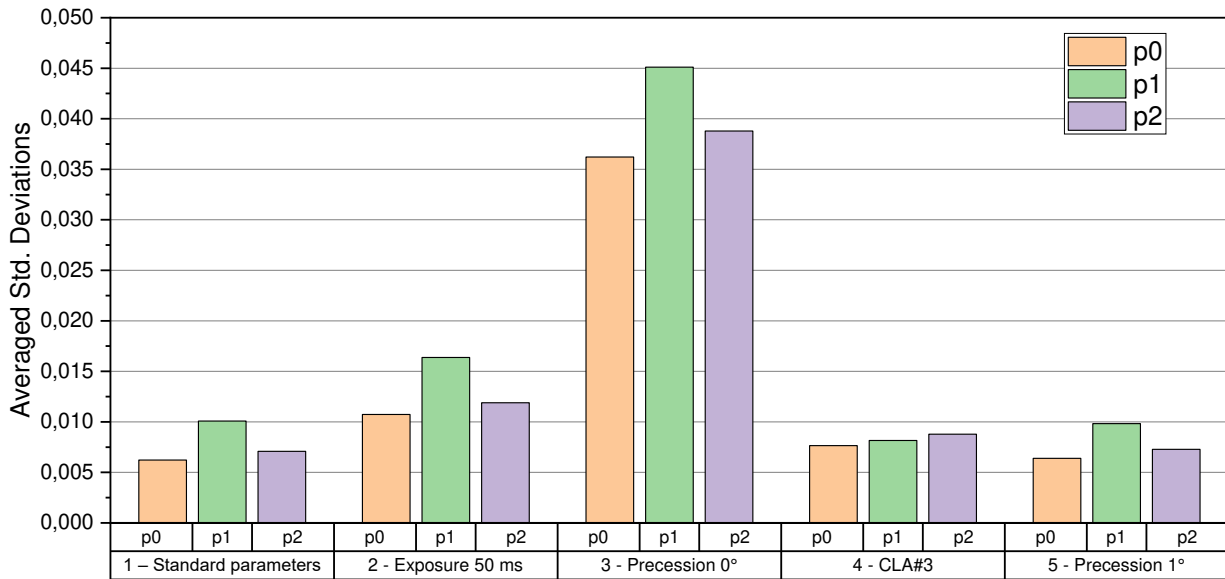
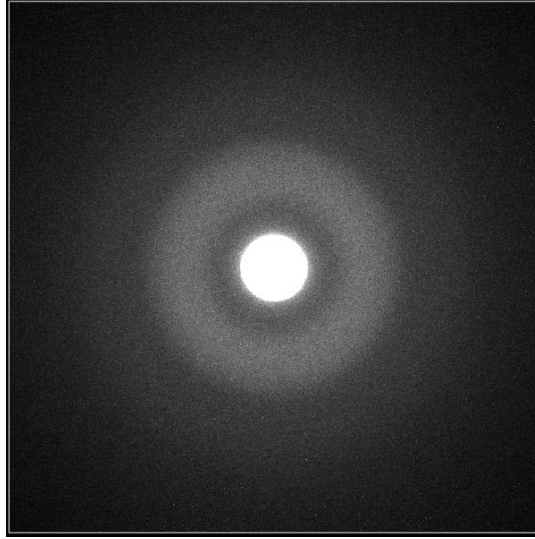


Figure 25: Averaged standard deviations of fitted parameters  $p_0$ ,  $p_1$  and  $p_2$  for each measurement.

The overview in Figure 25 already shows a clear trend, which is confirmed through the whole study: Measurement 3 shows the highest averaged standard deviation with 0.04, since no beam precession is being applied. Similarly, measurement 2, which was recorded using a shorter exposure time, has a higher averaged standard deviation of 0.01 in its fitted ellipticity parameters than the rest. Measurements 1 and 5 are showing the lowest spread in the fitted results, while differing only in precession angle. Measurement 1, with a precession angle of  $0.5^\circ$  shows averaged standard deviations of  $7.79\text{E-}3$ , similar to measurement 5, for which a precession angle of  $1^\circ$  was used, with an averaged standard deviation of  $7.80\text{E-}3$ . It can thus be concluded that a precession angle of  $0.5^\circ$  is sufficient for improving the intensity distribution of recorded amorphous ring patterns and thus fit accuracy.

Measurement 4 was the only one conducted using the condenser lens aperture 3 (CLA #3), which has a larger diameter than CLA #4. The movable condenser lens aperture, or C2 aperture is adjustable in discrete steps. A larger aperture increases the beam current and also the convergence angle of the beam [40]. Using CLA #3, instead of aperture #4 thus results in a more converged beam, which manifests itself in a broader ring pattern, as seen in Figure 26.



*Figure 26: Diffuse ring pattern from measurement 4, using CLA #3.*

The ellipticity parameters  $p_0$  and  $p_2$  show a higher averaged standard deviation in measurement 4, which can be attributed to the condenser lens aperture 3 (CLA #3). The broader ring pattern is expected to be more challenging to fit with a small residual error. Although the larger spread of measurement 4 could be mitigated using modified fitting parameters (e.g., a masked fit), overall, this measurement delivered more inconsistent results, compared to measurements 1 and 5.

### **4.3.2. Discussion of the Influence of Fitting Parameters**

The standard deviation of fitted parameters is again taken as a measure for fit precision. First, the averaged standard deviation for every fitting parameter set from Table 2 is shown in Figure 27. Analogous to the previous chapter, the standard deviations of fitted parameters  $p_0$ ,  $p_1$ , and  $p_2$  have now been averaged over all five measurements, revealing the influence of the different fitting parameters.

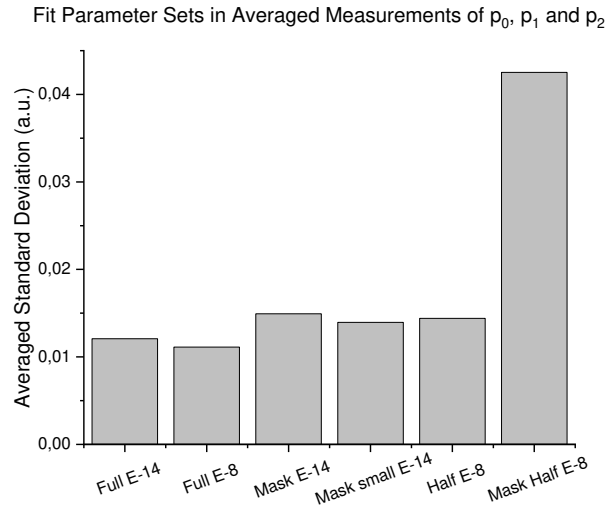


*Figure 27: Averaged standard deviations of the fitted ellipticity results  $p_0$ ,  $p_1$ , and  $p_2$ , which were averaged over all five measurements.*

The results from the different parameters used for data fitting, show that measures to improve fit accuracy or decrease processing times in many cases do not improve the standard deviations of the fit results, when analysing ellipticity. Furthermore, fits using very low RMS tolerance values ( $<1E-14$ ), do not indicate significantly more accurate fit results, than procedures using the standard RMS tolerance ( $<1E-8$ ). Using a mask to omit the direct beam or resizing the frame can greatly reduce processing time, with an increase in averaged standard deviation from  $1.12E-2$  for a full fit, to  $1.50E-2$  for a masked fit, an increase of around 30%. This may be acceptable for evaluation procedures, which are to provide a quick assessment of a 4D STEM map. However, the use of resizing and masking simultaneously impacts fit precision to such a degree, that no meaningful results might be refined. A clear worst-case scenario is caused when fitting a 4D STEM map, which was recorded without precession, using a fit procedure that uses resized frames and a full mask, yielding the highest standard deviations from all fitted results.

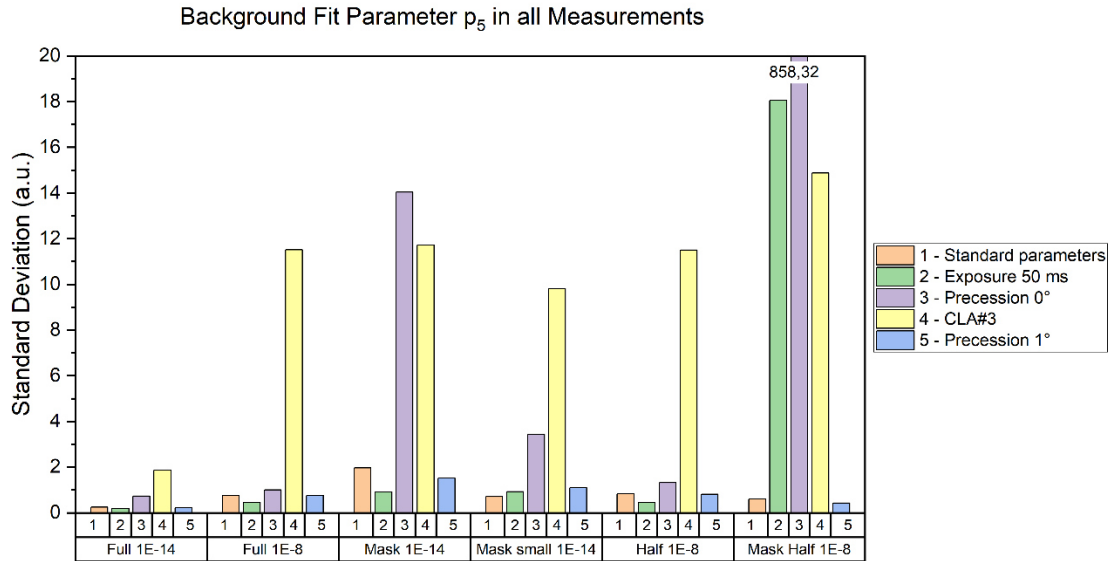


*Figure 28: Standard deviations of fitted background parameter  $p_5$  plotted for all fit procedures and measurements. Horizontal categories show the measurement number with the corresponding fitting parameter sets.*

This trend in fitting parameters holds especially true when considering background fit results, which can be of importance when also analysing composition of amorphous materials. It is obvious that background fitting is much more accurate, when using a full frame fit since a mask suppresses most of the information, except the halo ring pattern. Thus, if background information of the diffraction patterns is of interest, a full fit is necessary. In Figure 28, both full frame fits show a reasonably low standard deviation. Measurement 4 stands out notably with a higher standard deviation, which could be attributed to the used condenser lens aperture CLA #3. Still acceptable standard deviation can be observed in the “Half 1E-8”-fit, while higher standard deviations occur in all masked fits. The “Mask Half 1E-8”-fit shows the highest standard deviation, as expected.

### 4.3.3. Conclusion I

The parameter study clearly identifies a set of scanning and fitting parameters to be favourable. For scanning parameters, an exposure time of 100 ms appears to be sufficient for the microscope settings in this experiment, together with a beam precession angle of 0.5°. A further increase of the precession angle does not deliver results featuring significantly lower standard deviations. The study on fitting parameters shows, that no shortcuts exist for

obtaining superior fit precision, at a shortened processing time. All measures to make fitting of a 1024 x 1024 px frame faster, are indeed able to shorten the time to fit the 4D STEM dataset, however significant losses in fit accuracy were observed. Measures such as masking the frame and resizing to frame sizes smaller than 512 x 512 px, should solely serve for supplying quick overview results. For a final evaluation with emphasis on fit precision, a full fit of the unresized frame should be always performed, while an RMS tolerance of 1E-8 is sufficient. Owing to the fact that frame fitting of the parametric ellipse equation can be performed on multiple CPU cores, evaluation times are reasonably short, even for large 4D STEM maps, with high-resolution diffraction patterns.

The lowest averaged standard deviation of fitted ellipticity results with a value of 7.79E-3 was achieved using a full fit on the results of measurement 1. A similar averaged standard deviation of 7.80E-3 was found using a full fit on the results of measurement 5. The similarity in both standard deviations of fit parameters and the actual results, suggests that the scattering of data points is not caused by reaching the fit precision threshold. A more probable cause for such similar results of measurement 1 and 5, is that the intrinsic heterogeneity of the observed Cu-Zr-Al BMG material was measured. This means that a “hard-limit” in fit precision was not reached with the two most precise measurements, it was rather confirmed, that this experiment accomplished to measure the structural heterogeneity of the examined BMG, demonstrating the high spatial resolution of the method.

## 5. Strain Mapping on Multi-layered TFMG Samples

### 5.1. Introduction

In this chapter multi-layered TFMG samples are analysed. This has two aims, firstly it allows testing the resolution and precision of the 4D STEM method and subsequent evaluation and secondly amorphous samples with a multi-layered nanostructure are expected to have attractive properties that directly depend on their local structure. This requires precise nanoscale measurement of the local strain field. Specifically, heterogeneous amorphous structures can show good mechanical properties, since structural gradients in multi-layered materials hinder shear band formation and crack propagation.

The samples were synthesized by *Evertz et al.* [47] through magnetron sputtering in a combinatorial growth system on a Si substrate. The provided samples showed a multilayer structure consisting of two periodically alternating sublayers with different chemical composition. The composition in the Co-Ta-B MG system is described as  $(Co_{6.8\pm 3.9}Ta)_{100-x}B_x$ , while the layer compositions are specified as  $Co_{76\pm 2}Ta_{9\pm 1}B_{15\pm 2}$  and  $Co_{62\pm 2}Ta_{8\pm 1}B_{29\pm 2}$  respectively. The Co-Ta-B MG system shows an atomic bonding character strongly dependent on the B concentration. While it exhibits metallic bonds at B concentration below  $39\pm 5$  at. %, covalent bonding character of the material increases at higher B concentrations, where B atoms can form an icosahedral network. With changes in B concentration, structural changes also occur in the medium range order of the material.

Two samples were investigated showing the same composition but different thickness of individual sublayers. From the samples cross-sectional TEM lamellae were prepared by lift-out using a Zeiss AURIGA CrossBeam workstation. The lamellae were subsequently attached to a TEM grid and further thinned down to electron transparency.

### 5.2. Experiment and Evaluation

The two examined multilayer samples featured a sublayer thickness of 10 and 150 nm for sample A and B, respectively. The sample A was scanned with a scan size of 40 x 40 frames, using an exposure time of 40 ms and a step size of 1 nm. Scan for sample B was performed with a resolution of 150 x 150 frames, an exposure time of 40 ms, with a step size of 1.6 nm. A total number of 1600 frames was recorded for sample A and 22500 frames for Sample B,

each with a resolution of 512 x 512 px. The fitting was performed on unresized and unmasked frames, in order to ensure a high fit precision.

### 5.3. Results

The aim of the evaluation procedure was to resolve the morphology of the sublayers in samples A and B, the thickness of the transition layers between the sublayers (called further thickness of the interfaces) and the strain distribution across the individual sublayers.

The thicknesses of the interfaces in samples A and B were determined using the intensity profiles gathered from the generated VBF images (Figure 29). In the samples A and B, the interface thicknesses of  $\sim 7.2$  and 6.5 nm were evaluated, respectively, even though the thickness of sample A interface was challenging to quantify, since sub-layer thickness is in the range of interface width, as visible in Figure 30.

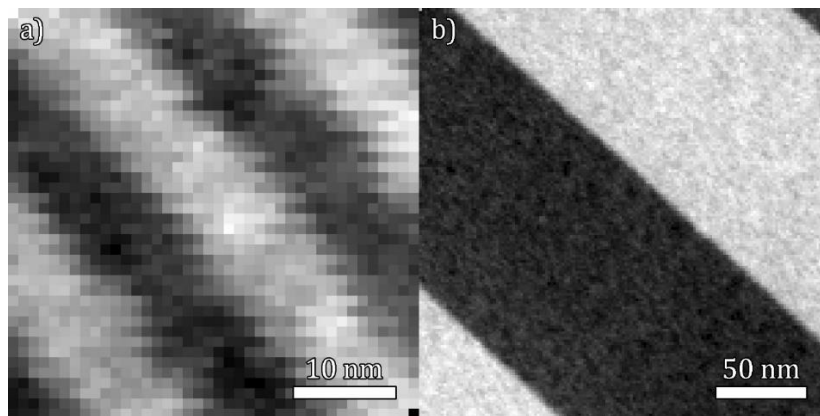


Figure 29: VBF micrographs of sample A (a) and sample B (b), showing the alternating multilayer structure with differing sublayer thickness.

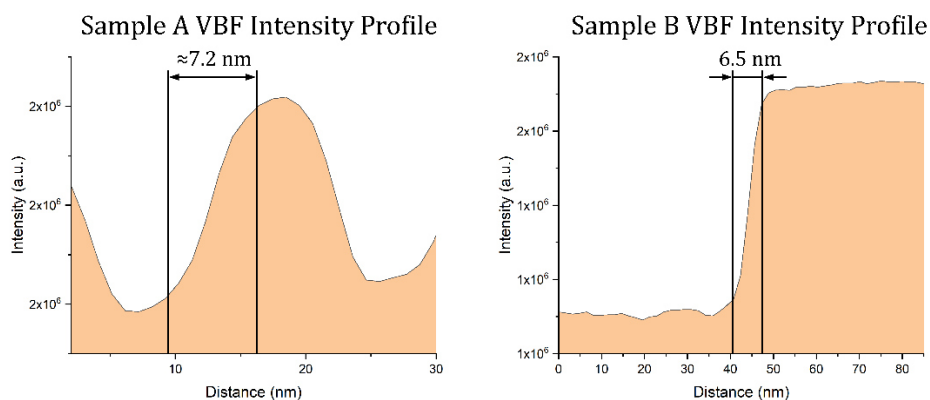


Figure 30: Intensity profiles calculated from VBF micrographs, showing sub-layer interface width.



Fit parameter results reveal strain, structural and compositional information of the scanned sample area. While a large amount of fitted and calculated parameters was obtained, only parameters necessary for a thorough material characterization will be presented hereafter. Strain information can be extracted from the fitted ellipticity parameters  $p_0$ ,  $p_1$ , and  $p_2$ , from which the two-dimensional strain tensor containing strains  $\varepsilon_{xx}$ ,  $\varepsilon_{xy}$  and  $\varepsilon_{yy}$  can be calculated using Eq. 6. The strain tensor is oriented in the direction to the layer interfaces, to show principal strains lying parallel and perpendicular to the interfaces of the individual layers. To achieve this, a rotational transformation of the strain tensor by  $+27^\circ$  for sample A and  $+33^\circ$  for sample B using Eq. 8 is necessary. With this rotation applied, strain component  $\varepsilon_{xx}$  lies perpendicular to the sublayer interfaces, while  $\varepsilon_{yy}$  lies parallel to the interfaces. The obtained maps for measurement of sample B were smoothed using a gaussian filter with a sigma value of 0,4 for better readability.

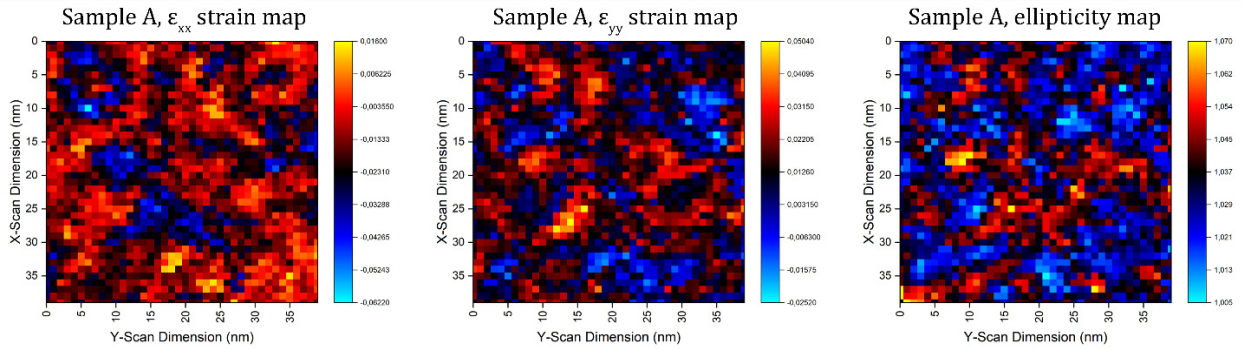


Figure 31: Strain maps of sample A showing calculated strain  $\varepsilon_{xx}$  (left), calculated strain  $\varepsilon_{yy}$  (center) and calculated ellipticity  $e$  (right).

The ellipticity value in Figure 31 is calculated from fitted ellipticity parameters  $p_0$ ,  $p_1$  and  $p_2$  using Eq. (9). It shows ellipticity of the diffraction pattern as a single value. A diffraction pattern from unstrained material with no ellipticity is showing a value of  $e = 1$ .

$$e = \sqrt{\frac{a+c+\sqrt{(a-c)*2+b*2}}{a+c-\sqrt{(a-c)*2+b*2}}} \quad (9)$$

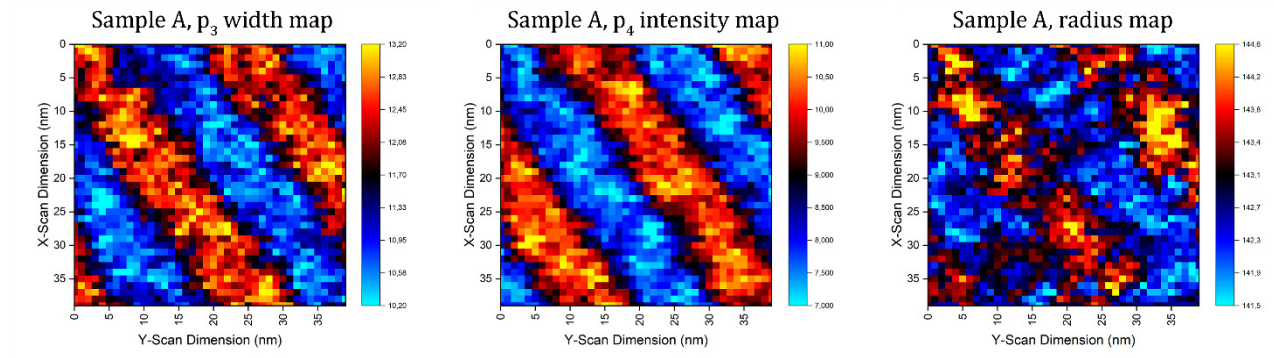


Figure 32: Strain maps of sample A showing fitted ring width  $p_3$  (left), fitted ring intensity  $p_4$  (center) and calculated ring radius  $r$  (right).

Structural and compositional information about the multi-layered microstructure is evaluated from the width and intensity of the amorphous ring, corresponding to the fitted parameters  $p_3$  and  $p_4$ , respectively (Figure 32). The mean radius  $r$  of the fitted ellipse can be derived using the unstrained radius  $r_0$ , as well as the ellipticity parameters in the following equation:

$$r = \frac{r_0}{\sqrt{4 \cdot p_0 \cdot p_2 - p_1^2}} / \sqrt{2} \cdot \left( \sqrt{p_0 + p_2 + \sqrt{(p_0 - p_2)^2 + p_1^2}} + \sqrt{p_0 + p_2 - \sqrt{(p_0 - p_2)^2 + p_1^2}} \right) \quad (10)$$

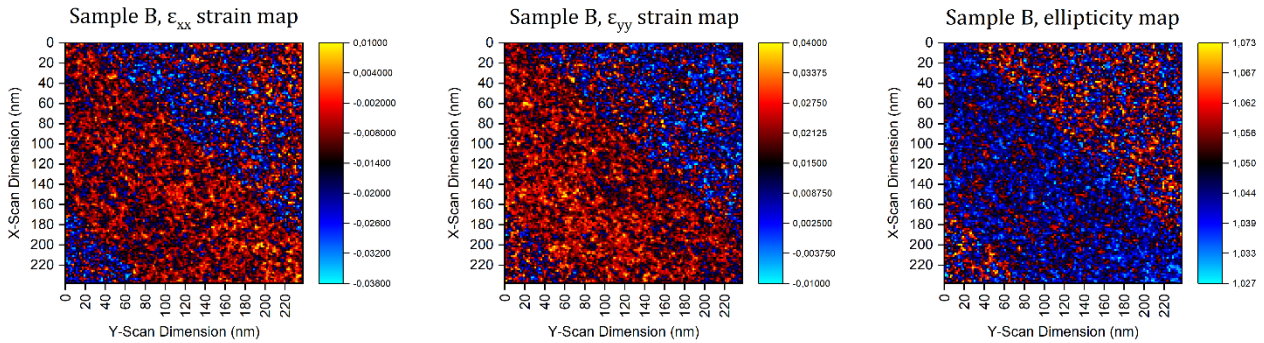


Figure 33: Strain maps of sample B showing calculated strain  $\epsilon_{xx}$  (left) and strain,  $\epsilon_{yy}$  (centre) and ellipticity  $e$  (right).

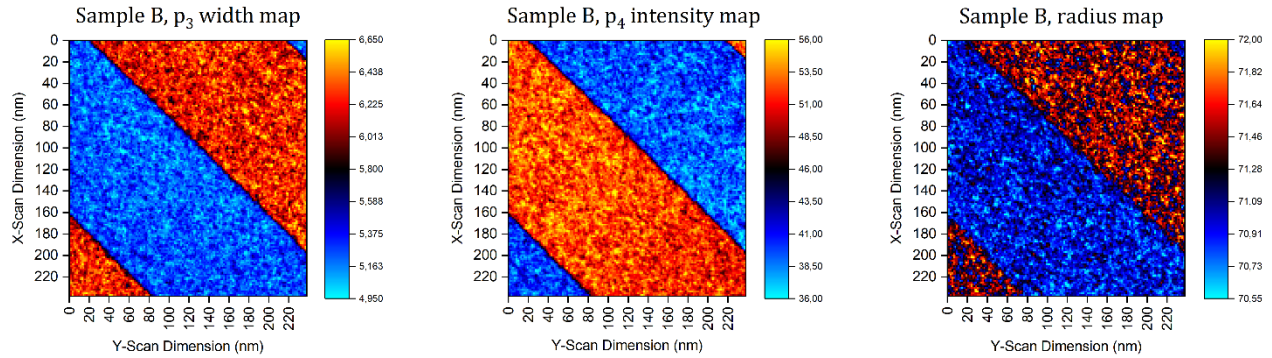


Figure 34: Strain maps of sample B showing fitted ring width  $p_3$  (left), intensity  $p_4$  (centre) and radius  $r$  (right).

## 5.4. Discussion

Overall, a sharp interface between the individual sublayers can be observed for sample B in Figure 30. The measured interface width in sample A is only a rough estimate, since sublayer thickness has similar dimensions.

Strain calculation and mapping does not show pronounced strain concentration on sub-layer interfaces and no significant in-plane and out-of-plane strains are present in the observed area. This is confirmed by the ellipticity parameter  $e$ , which is not significantly increased at the interface vicinity, as visible in Figure 31 and Figure 33.

The varying Boron content of the individual sublayers of both samples is confirmed by the fitted results. Considering the VBF images (Figure 29), the sub-layer with higher B content can be identified by its lower intensity in the BF, since a lower fraction of elements with high atomic number  $Z$  is present. Fitted ellipse ring intensity, which is supplied by fit parameter  $p_4$  (Figure 32 and Figure 34), contains information about sublayer composition. A higher atomic number  $Z$  leads to a higher amount of elastically scattered electrons, which can cause a higher diffraction pattern ring intensity, although structural factors need to be accounted for. Considering the composition of  $(Co_{6.8\pm 3.9}Ta)_{100-x}B_x$ , a higher B content leads to decreased Co and Ta contents, which both possess a considerably higher  $Z$  than B. It thus can be expected that the B-rich sublayers exhibit a lower ring intensity than the sublayers which have low B contents, as confirmed in Figure 32 and Figure 34. Furthermore, results from Evertz et al. show peak broadening of the obtained structure factor with increasing B content.

This is reflected by the fitted ring width parameter  $p_3$ , which is also higher in the sublayers with increased B content, visible in Figure 32 and Figure 34.

A structural difference between individual sublayers is revealed by the radius  $r$  of the fitted ellipse, which is derived using Eq. 10, with its distribution visible in Figure 32 and Figure 34. The radius of the ellipse is inversely proportional to the mean atomic distance of the diffracted material, which is comparable to the first maximum in an atomic distribution function in real space. Since the scattering intensity is inversely proportional to the mean atomic distance, higher values of  $r$  indicate a smaller mean atomic distance and vice-versa. The suspected increase in mean atomic distance in B rich sublayers could not be observed in the evaluated data. Both multi-layered structures however feature a similar spread of the mean atomic distance in the observed area. The percentual difference of fitted ellipse radius  $r$  can be calculated to 2.2% in sample A and 2.1% in sample B.

## 5.5. Conclusion II

The evaluated measurements give insights into the structure and composition of the sublayers, as well as strain distributions at the interfaces. The resulting strain maps show no pronounced strain concentration at the interfaces. This confirms that amorphous interfaces do not feature significant directional strain due to a mismatch of mean atomic distances. On interfaces of two crystal lattices with differing lattice constants, a misfit strain is observed on coherent interfaces, together with the possible formation of misfit dislocations on a semi-coherent interface. Solids missing an ordered atomic arrangement or a definable lattice constant, do not possess interfacial strain, as visible in Figure 35.

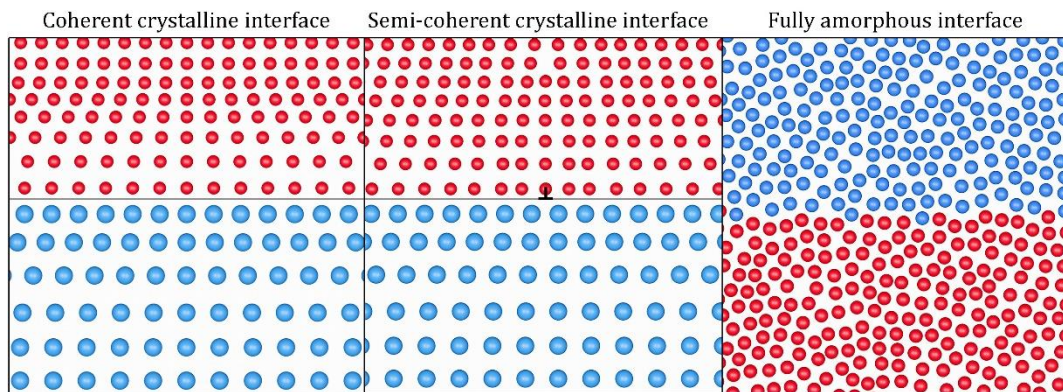


Figure 35: A schematic representation of crystalline and amorphous interfaces.

The 4D STEM method thus grants unique insight into strain distribution in nanostructured multi-layered amorphous materials with nanometre resolution. Characterization methods using larger probe sizes on the other hand, only obtain a mean value with limited spatial resolution, which prevents from making definite statements about interfacial strains and structure. Thanks to the small probe size, the method also allows to evaluate interface width.

The obtained results for mean atomic distance fluctuations of roughly 2% in both samples show, that pronounced structural gradients are achievable at sublayer thicknesses of 10 nm, as found in sample A. This sample features interfaces with roughly double the width of the sublayer thickness (Figure 30), which results in a strong structural gradient. For mechanical properties of multi-layered amorphous structures, it can be expected that a sublayer thickness, which lie in the size range of the interface width, form an ideal structure against strain localization, preventing formation of shear bands, which is the underlying plastic deformation mechanism in MGs.

It was also attempted to gather structural information from the calculated ellipse radius, which could allow identifying sublayers which are low on B or B rich. According to *Evertz et al.* [47], the addition of B to the material increases the mean atomic bond length between metallic (Co and Ta) and B atoms  $r_{M-B}$ , as well as between metallic atoms  $r_{M-M}$ . This would lead to a peak shift of the RDF, as well as shift of the structure factor, which should correlate to the calculated radius results. It should be noted however, that considerable shifts only occurred at higher B concentrations, above roughly 50%. After a comparison to the specified B contents in the sublayers it is improbable, that a peak shift due to B concentration differences is measurable, since the B content fluctuation is below 50%.

## 6. In-situ strain mapping of a MG bending beam during loading

### 6.1. Introduction

The 4D STEM method was used to perform strain mapping during an in-situ bending beam (micro-cantilever) experiment, with subsequent evaluation by ellipse fitting of the obtained NBED patterns. Several bending beams were machined at the micrometre scale in a Zeiss AURIGA CrossBeam workstation from a  $Cu_{46}Zr_{46}Al_8$  BMG material using FIB. This material is known for its good mechanical properties and is widely used technologically, as mentioned in Chapter 4.1. The first experiment was performed on bending beams, with a notch cut using electron beam lithography inside the TEM. This type of notch creation method however proved to be time consuming, since the sputter rate through electron beam induced irradiation was not high enough to produce a sizeable notch in an adequate timeframe. Experiments using such small notches did not deliver the expected strain distributions, since the notch was too small to induce measurable local stress. Thus, additional bending beam specimens were machined and the notch was directly introduced by FIB milling.

### 6.2. Experiment

Scan dimensions for this measurement were selected with the aim of generating high-resolution 4D STEM datasets. Using a scan resolution of 180 x 180, 32400 frames were recorded in total, each with a resolution of 512 x 512 px. A precession angle of 0.5° was used, together with an exposure time of 10 ms per frame and a step size of approximately 2 nm.

During scanning, the bending beam was loaded by a wedge indenter using a Hysitron PI95 picoindenter holder (Figure 36a). First, a 4D STEM measurement was performed on the unloaded sample. Subsequently, the indenter was brought into contact with the sample while monitoring the force. In total, four separate maps were captured at different indenter displacements. The set displacements of 0, 20, 28 and 32 nm were maintained by the indenter varying only by approximately 0.2 nm, as shown in Figure 36b. The generated strain fields are be labelled for the set displacements.

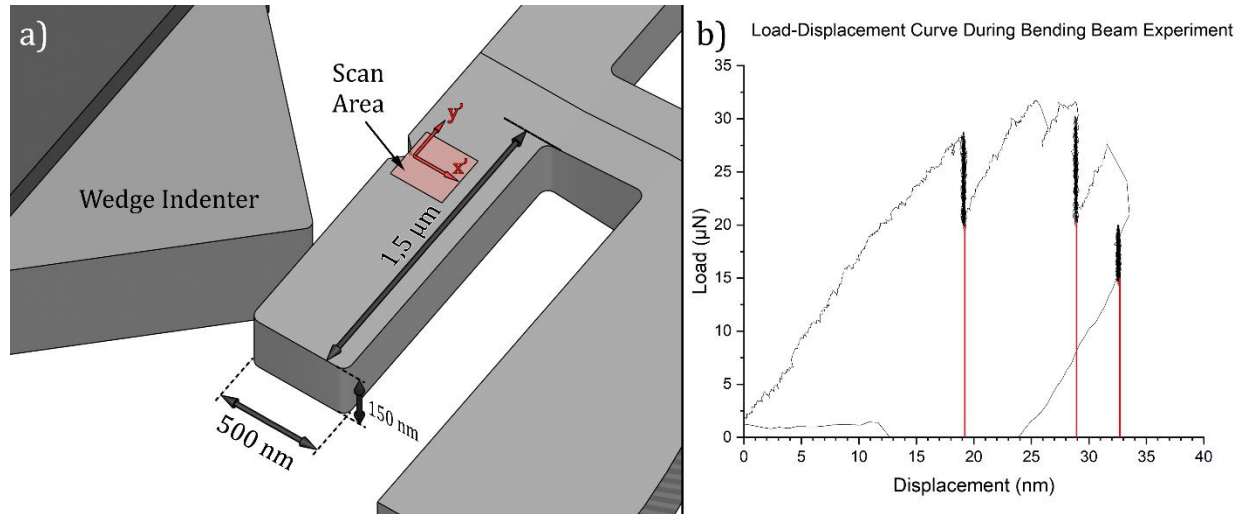


Figure 36: (a) Geometry of the in-situ loading experiment, with dimensions of the bending beam, showing the orientation of principal axes  $[x', y']$  for strain analysis. The marked scan area is an approximation and prone to shift during loading of the sample. (b) Load-displacement curve of the indenter during loading, showing the three different holding points.

It should be noted that the scan area does not capture the identical sample region at each displacement step, since the bending beam can deflect during loading. Due to relaxation effects and drift during scanning, the scan does not maintain a perfectly stationary region of the material.

### 6.3. Evaluation

For strain analysis, the strains were calculated from fitted ellipticity parameters  $p_0$ ,  $p_1$ , and  $p_2$  using Eq. 6. The calculated strain tensor needs to be transformed by rotation, to show strain fields of principal strains  $\varepsilon_{xx}$ ,  $\varepsilon_{xy}$  and  $\varepsilon_{yy}$  in the orientation of the bending beam, as opposed to the scanning orientation. The quadratic scanned area is rotated to the longitudinal axis of the bending beam by a total of  $-21^\circ$ . The recorded NBED patterns are however already rotated by  $-14^\circ$  with respect to the scanning coordinates  $x^s$  and  $y^s$  and also determine the orientation of the initially evaluated strain tensor. The remaining necessary transformation to match the bending beam coordinates  $x'$  and  $y'$  is thus  $-7^\circ$ . The rotated  $y$ -axis then points parallel to the longitudinal  $y'$ -axis of the beam, while the  $x$ -axis is rotated to point in the direction of the wedge opening,  $x'$ . This transformation is visible in Figure 37 (all axes are perpendicular to the incident electron beam).

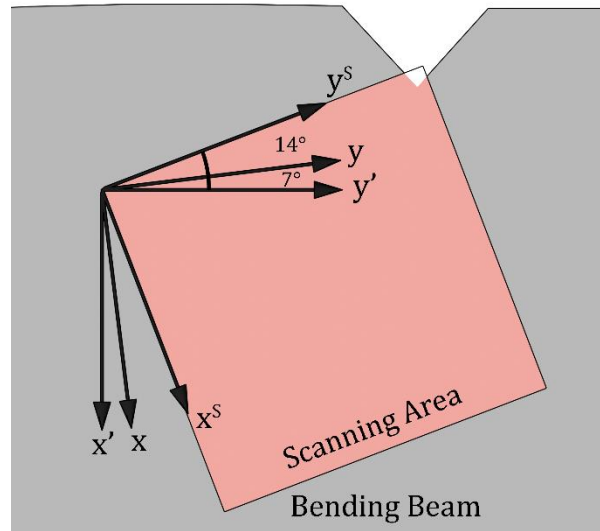


Figure 37: Transformation of the coordinate system: The orientation of the bending beam coordinate system  $x', y'$  is rotated by  $-7^\circ$  to the orientation of recorded NBED patterns  $x, y$  and by  $-21^\circ$  to the scanning area coordinates  $x^s, y^s$ .

#### 6.4. Results

The following strain fields (Figure 38, Figure 39, Figure 40) show principal strains in the orientation of the bending beam  $x', y'$  for all four measured displacements. The plots have been smoothed using a gaussian filter with a sigma value of 0.7, to improve readability. The arithmetic mean value of unloaded strain fields has been subtracted from all corresponding loaded strain fields, to correct for the small elliptic distortion attributed to the microscope and only take into account the strain increase during loading.



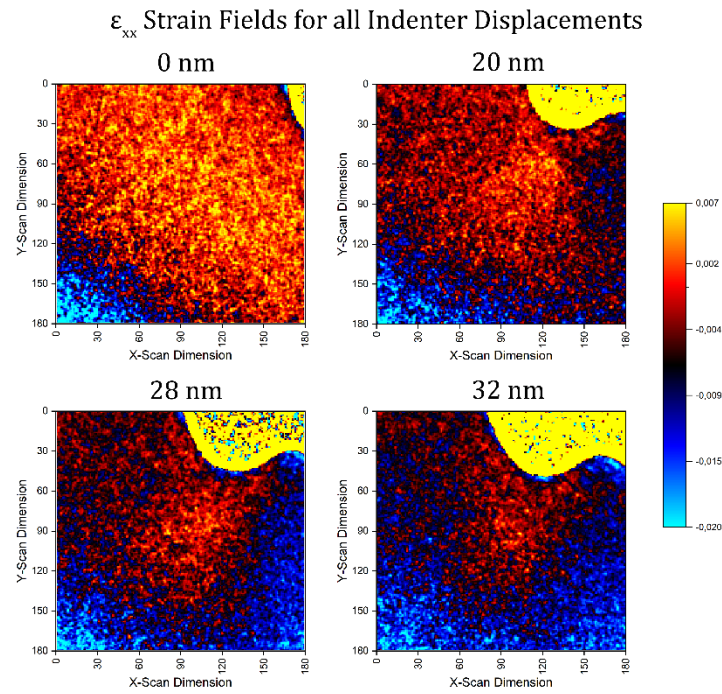


Figure 38: Strain fields of  $\epsilon_{xx}$  for all recorded indenter displacements during bending beam loading.

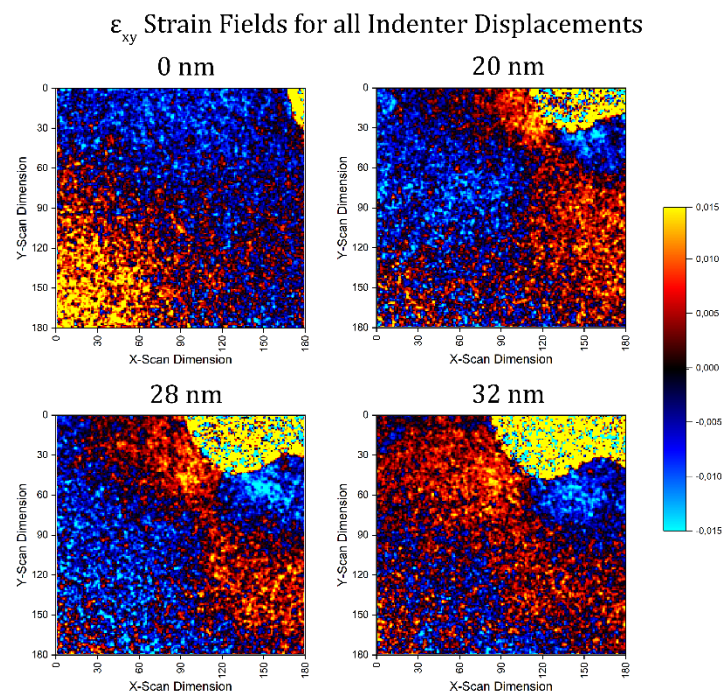


Figure 39: Strain fields of  $\epsilon_{xy}$  for all recorded indenter displacements during bending beam loading.

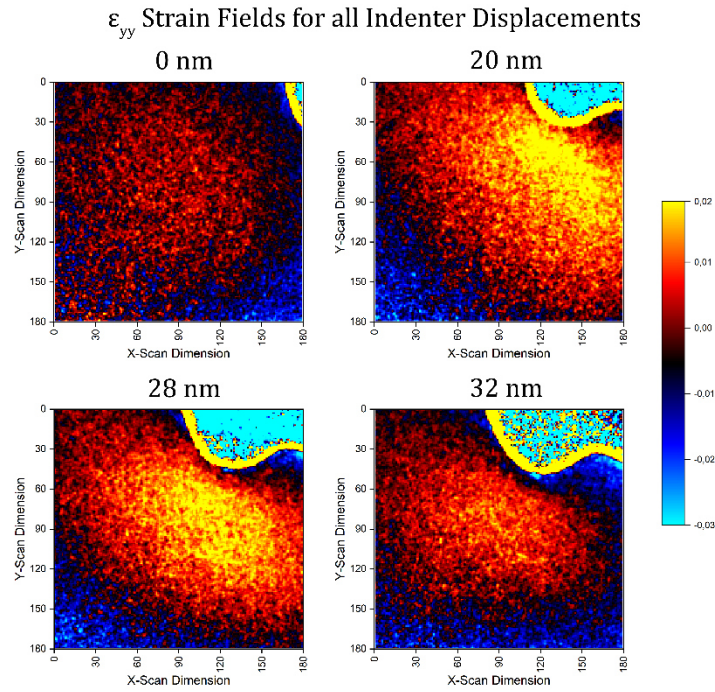


Figure 40: Strain fields of  $\epsilon_{yy}$  for all recorded indenter displacements during bending beam loading.

## 6.5. Discussion

The resulting strain fields show a pronounced strain concentration at the tip of the notch. As indicated by the load displacement curve in Figure 36b, the elastic region is maintained until the first loaded measurement at 20 nm. The obtained results overall agree with strain fields from notched BMG bending beam experiments on larger beam geometries from Ref. [48]. Strain intensities indicate a load falloff at the subsequent 28 and 32 nm measurements, which is confirmed by the load displacement data of the indenter (Figure 36b). The  $\epsilon_{xx}$  strain component in the 0 nm measurement shows negative values in the lower-left edges, which does not correspond to the expected strain distribution. A possible explanation is obscuring of frames through the beam stop in the corresponding region.

## 6.6. Conclusion III

The evaluated strain maps are mostly in agreement with theoretical descriptions of strain distributions of notched bending beam experiments. From beginning of the indenter displacement, a linear strain increase is expected, with plastic deformation at the tip of the notch. Up to the 20 nm measurement, the material is within the elastic range, with

pronounced strain fields in the 20 nm maps. At higher loads, plastic deformation is occurring, which can be described by the formation of shear transformation zones (STZ), as well as the accumulation of free volume in the MG. Generally, areas in the materials can undergo softening upon plastic deformation, causing strain localization to occur. Strain maps obtained at 28 and 32 nm displacement show more diffuse strain fields and a smaller maximum strain, which would indicate a locally more soft material [49].

In theory, the distribution of the crack-opening strain should assume a “butterfly”-shape [48]. This distribution is visible in the  $\varepsilon_{yy}$  strain component in Figure 40, which is showing an oval distribution, featuring asymmetry with respect to the notch. The deviation from the theoretical shape can be first and foremost attributed to the blunt and also potentially asymmetrical notch geometry, as well as uneven contact of the indenter. The shear strain component  $\varepsilon_{xy}$  forms a distribution featuring lobes with a negative four-fold rotational symmetry (*cf.* Figure 39), which can also be attributed to the asymmetrical conditions of load application. For the strain distribution  $\varepsilon_{xx}$  in notch direction, the highest values are observed in the 0nm strain map (*cf.* Figure 38), which would not correspond to the unloaded state of the bending beam. An explanation could be the fact that the unloaded state was measured before the series of the other maps was taken. Therefore, there is the possibility that a change in microscope parameters after the first measurement occurred, namely camera length, which would lead to an offset in the strain value.

Overall, the experiment showed the capabilities of acquiring 4D STEM maps on in-situ experiments, resolving local elastic strain evolution with high a spatial resolution. In addition, it demonstrated the transition from purely elastic strain around the notch to local softening manifesting itself in a broader strain distribution. Improvements in the execution of the experiment remain to be implemented, namely improving the notch sharpness and acquiring more maps. This should allow to obtain more quantitative strain distributions at different loads, which can be quantitatively compared with simulations.

## 7. Summary

The thesis presented a data evaluation procedure of 4D STEM datasets of MGs through fitting of a two-dimensional parametric function. The NBED method in STEM operating mode was described, with an emphasis on the formation and interpretation of singular NBED patterns, together with the influence of electron beam precession. The information contained in NBED patterns and the possibility of deriving local atomic strains was illustrated. Data processing steps of the acquired NBED patterns were presented, as well as the programmatic implementation of evaluation through fitting of a parametric function in python. The conducted parameter study on a Cu-Zr-Al BMG highlighted the importance of electron beam precession during measurement, which allows a straightforward and precise evaluation with high spatial resolution. The study also revealed optimal parameters for high fit precision, which requires unresized, as well as unmasked NBED frames, with adequate resolution. Results of highest precision measurements proved that the method is suitable to measure the intrinsic heterogeneity of MGs. High fit precision also involves higher computational workload, which is however acceptable when using the multiprocessing implementation of the data fitting procedure. Utilizing fast electron detectors for capturing NBED patterns, together with high-bandwidth storage, allows capturing 4D STEM datasets with large dimensions. An improvement in processing speed would be expected with the implementation of GPU-accelerated fitting of the parametric ellipse function. The analysis of a  $(Co_{6.8\pm 3.9}Ta)_{100-x}B_x$  multi-layered TFMG sample proved 4D STEM strain mapping and the presented evaluation approach to be a suitable method for nanoscale characterization of amorphous metallic alloys, revealing strain distributions at amorphous interfaces. The fully amorphous multilayers could be resolved with nanometre resolution, providing information about structure and composition of individual sublayers. Evaluated 4D STEM datasets acquired during an in-situ bending beam experiment of a Cu-Zr-Al BMG yielded strain fields, that reveal strain concentration around the introduced notch. Resulting strain maps are furthermore corresponding to the load displacement curve of the indenter. This confirms that the method, with its subsequent evaluation procedure is able to quantitatively map strain distributions in fully amorphous materials with nanometre resolution.

## 8. References

- [1] C. Gammer, C. Ophus, T.C. Pekin, J. Eckert, A.M. Minor, Local nanoscale strain mapping of a metallic glass during in situ testing, *Appl. Phys. Lett.* 112 (2018). <https://doi.org/10.1063/1.5025686>.
- [2] W. Klement, R.H. Willens, P. Duwez, Non-crystalline structure in solidified Gold-Silicon alloys, *Nature*. 187 (1960) 869–870. <https://doi.org/10.1038/187869b0>.
- [3] A.L. Greer, *Metallic Glasses*, *Phys. Metall.* Fifth Ed. 1 (2014) 305–385. <https://doi.org/10.1016/B978-0-444-53770-6.00004-6>.
- [4] J.P. Chu, J.S.C. Jang, J.C. Huang, H.S. Chou, Y. Yang, J.C. Ye, Y.C. Wang, J.W. Lee, F.X. Liu, P.K. Liaw, Y.C. Chen, C.M. Lee, C.L. Li, C. Rullyani, Thin film metallic glasses: Unique properties and potential applications, *Thin Solid Films*. 520 (2012) 5097–5122. <https://doi.org/10.1016/j.tsf.2012.03.092>.
- [5] C. Suryanarayana, A. Inoue, *Bulk metallic glasses: Second edition*, 2017. <https://doi.org/10.1201/9781315153483>.
- [6] J.D. Musgraves, J. Hu, L. Calvez, *Springer Handbook of Glass*, Springer International Publishing, Cham, 2019. <https://doi.org/10.1007/978-3-319-93728-1>.
- [7] L. Zhong, J. Wang, H. Sheng, Z. Zhang, S.X. Mao, Formation of monatomic metallic glasses through ultrafast liquid quenching, *Nature*. 512 (2014) 177–180. <https://doi.org/10.1038/nature13617>.
- [8] C. Suryanarayana, A. Inoue, *Metallic Glasses*, in: *Ullmann's Encycl. Ind. Chem.*, Wiley-VCH Verlag GmbH & Co. KGaA, Weinheim, Germany, 2012: pp. 305–385. [https://doi.org/10.1002/14356007.a16\\_335.pub2](https://doi.org/10.1002/14356007.a16_335.pub2).
- [9] Z.P. Lu, C.T. Liu, A new glass-forming ability criterion for bulk metallic glasses, *Acta Mater.* 50 (2002) 3501–3512. [https://doi.org/10.1016/S1359-6454\(02\)00166-0](https://doi.org/10.1016/S1359-6454(02)00166-0).
- [10] A. Inoue, Recent progress of Zr-based bulk amorphous alloys, *Sci. Reports Research Institutes Tohoku Univ. Ser. A-Physics*. 42 (1996) 1–11.
- [11] E.J. Lavernia, T.S. Srivatsan, *The rapid solidification processing of materials: Science, principles, technology, advances, and applications*, *J. Mater. Sci.* 45 (2010) 287–325.

- <https://doi.org/10.1007/s10853-009-3995-5>.
- [12] M. Bakkal, U. Karagüzel, A.T. Kuzu, Manufacturing Techniques of Bulk Metallic Glasses, *Mod. Manuf. Process.* (2019) 137–148. <https://doi.org/10.1002/9781119120384.ch6>.
- [13] A. Inoue, N. Nishiyama, H. Kimura, Preparation and thermal stability of Bulk Amorphous Pd<sub>40</sub>Cu<sub>30</sub>Ni<sub>10</sub>P<sub>20</sub> alloy cylinder of 72 mm in diameter, *Mater. Trans.* 38 (1997) 179–183.
- [14] R.C. Budhani, T.C. Goel, K.L. Chopra, Melt-spinning technique for preparation of metallic glasses, *Bull. Mater. Sci.* 4 (1982) 549–561. <https://doi.org/10.1007/BF02824962>.
- [15] T. Bitoh, D. Shibata, Improvement of soft magnetic properties of [(Fe<sub>0.5</sub>Co<sub>0.5</sub>)<sub>0.75</sub>B<sub>0.20</sub>Si<sub>0.05</sub>]<sub>96</sub>Nb<sub>4</sub> bulk metallic glass by B<sub>2</sub>O<sub>3</sub> flux melting, *J. Appl. Phys.* 103 (2008) 1–4. <https://doi.org/10.1063/1.2829012>.
- [16] J. Schroers, T. Nguyen, S. O’Keeffe, A. Desai, Thermoplastic forming of bulk metallic glass-Applications for MEMS and microstructure fabrication, *Mater. Sci. Eng. A.* 448–451 (2007) 898–902. <https://doi.org/10.1016/j.msea.2006.02.398>.
- [17] D.M. Mattox, *Deposition ( PVD ) Processing Second edition Dedication To my wife Vivienne,* 2009. [http://www.elsevier.com/wps/find/bookdescription.cws\\_home/717814/description#description](http://www.elsevier.com/wps/find/bookdescription.cws_home/717814/description#description).
- [18] A. Hutagalung, *High Power Impulse Magnetron Sputtering,* Elsevier, 2020. <https://doi.org/10.1016/C2016-0-02463-4>.
- [19] K. Wasa, *Handbook of Sputtering Technology,* Elsevier, 2012. <https://doi.org/10.1016/C2010-0-67037-4>.
- [20] I. Petrov, P.B. Barna, L. Hultman, J.E. Greene, Microstructural evolution during film growth, *J. Vac. Sci. Technol. A Vacuum, Surfaces, Film.* 21 (2003) S117–S128. <https://doi.org/10.1116/1.1601610>.
- [21] P.B. Barna, M. Adamik, Fundamental structure forming phenomena of polycrystalline films and the structure zone models, *Thin Solid Films.* 317 (1998) 27–33.

- [https://doi.org/10.1016/S0040-6090\(97\)00503-8](https://doi.org/10.1016/S0040-6090(97)00503-8).
- [22] J. A. Thornton, High rate thick film growth, *Annu. Rev. Mater. Sci.* 7 (1977) 239.
- [23] P. Luo, C.R. Cao, F. Zhu, Y.M. Lv, Y.H. Liu, P. Wen, H.Y. Bai, G. Vaughan, M. Di Michiel, B. Ruta, W.H. Wang, Ultrastable metallic glasses formed on cold substrates, *Nat. Commun.* 9 (2018). <https://doi.org/10.1038/s41467-018-03656-4>.
- [24] D.P.B. Aji, A. Hirata, F. Zhu, L. Pan, K.M. Reddy, Y. Liu, T. Fujita, S. Kohara, M. Chen, Ultrastable and Ultrastrong Glass, (n.d.) 1–24.
- [25] J.P. Chu, C.T. Liu, T. Mahalingam, S.F. Wang, M.J. O’keefe, B. Johnson, C.H. Kuo, Annealing-induced full amorphization in a multicomponent metallic film, *Phys. Rev. B - Condens. Matter Mater. Phys.* 69 (2004) 1–4. <https://doi.org/10.1103/PhysRevB.69.113410>.
- [26] Q. Zeng, H. Sheng, Y. Ding, L. Wang, W. Yang, J.Z. Jiang, W.L. Mao, H.K. Mao, Long-range topological order in metallic glass, *Science* (80-. ). 332 (2011) 1404–1406. <https://doi.org/10.1126/science.1200324>.
- [27] X. Yue, A. Inoue, C.T. Liu, C. Fan, The development of structure model in metallic glasses, *Mater. Res.* 20 (2017) 326–338. <https://doi.org/10.1590/1980-5373-MR-2016-0318>.
- [28] J.D. Bernal, The Bakerian Lecture, 1962 The structure of liquids, *Proc. R. Soc. London. Ser. A. Math. Phys. Sci.* 280 (1964) 299–322. <https://doi.org/10.1098/rspa.1964.0147>.
- [29] Y. Waseda, H.-S. Chen, K. Thomas Jacob, H. Shibata, On the glass forming ability of liquid alloys, *Sci. Technol. Adv. Mater.* 9 (2008) 023003. <https://doi.org/10.1088/1468-6996/9/2/023003>.
- [30] J.L. Finney, Bernal’s road to random packing and the structure of liquids, *Philos. Mag.* 93 (2013) 3940–3969. <https://doi.org/10.1080/14786435.2013.770179>.
- [31] J.D. BERNAL, Geometry of the Structure of Monatomic Liquids, *Nature.* 185 (1960) 68–70. <https://doi.org/10.1038/185068a0>.
- [32] H. Lou, Z. Zeng, F. Zhang, S. Chen, P. Luo, X. Chen, Y. Ren, V.B. Prakapenka, C. Prescher, X. Zuo, T. Li, J. Wen, W.H. Wang, H. Sheng, Q. Zeng, Two-way tuning of structural order in metallic glasses, *Nat. Commun.* 11 (2020). <https://doi.org/10.1038/s41467-019->

- 14129-7.
- [33] R.E. Dinnebier, S.J.L. Billinge, eds., Powder Diffraction, The Royal Society of Chemistry, 2008. <https://doi.org/10.1039/9781847558237>.
- [34] W.H. Wang, The nature and properties of amorphous matter, *Prog. Phys.* 33 (2013) 177–351.
- [35] D.B. Miracle, The density and packing fraction of binary metallic glasses, *Acta Mater.* 61 (2013) 3157–3171. <https://doi.org/10.1016/j.actamat.2013.02.005>.
- [36] W. Hume-Rothery, H.M. Powell, On the Theory of Super-Lattice Structures in Alloys, *Zeitschrift Für Krist. - Cryst. Mater.* 91 (1935) 23–47. <https://doi.org/10.1524/zkri.1935.91.1.23>.
- [37] D.B. Miracle, A physical model for metallic glass structures: An introduction and update, *Jom.* 64 (2012) 846–855. <https://doi.org/10.1007/s11837-012-0359-4>.
- [38] R. Babilas, K. Cesarz-Andraczke, D. Babilas, W. Simka, Structure and Corrosion Resistance of Ca<sub>50</sub>Mg<sub>20</sub>Cu<sub>30</sub> Bulk Metallic Glasses, *J. Mater. Eng. Perform.* 24 (2015) 167–174. <https://doi.org/10.1007/s11665-014-1308-x>.
- [39] M. Stoica, J. Das, J. Bednarcik, H. Franz, N. Mattern, W.H. Wang, J. Eckert, Strain distribution in Zr<sub>64.13</sub>Cu<sub>15.75</sub>Ni<sub>10.12</sub>Al<sub>10</sub> bulk metallic glass investigated by in situ tensile tests under synchrotron radiation, *J. Appl. Phys.* 104 (2008). <https://doi.org/10.1063/1.2952034>.
- [40] D.B. Williams, C.B. Carter, *Transmission Electron Microscopy*, Springer US, Boston, MA, 2009. <https://doi.org/10.1007/978-0-387-76501-3>.
- [41] N. Van Steenberge, Study of structural changes in Zr-based bulk metallic glasses upon annealing and deformation treatments, (2008) 241.
- [42] P. Jia, J.M. Liu, E.G. Wang, K. Han, The effects of high magnetic field on crystallization of Fe<sub>71</sub>(Nb<sub>0.8</sub>Zr<sub>0.2</sub>)<sub>6</sub>B<sub>23</sub> bulk metallic glass, *J. Alloys Compd.* 581 (2013) 373–377. <https://doi.org/10.1016/j.jallcom.2013.07.066>.
- [43] P.D. Nellist, S.J. Pennycook, The principles and interpretation of annular dark-field Z-contrast imaging, 2000. [https://doi.org/10.1016/S1076-5670\(00\)80013-0](https://doi.org/10.1016/S1076-5670(00)80013-0).



- [44] C.R. Harris, K.J. Millman, S.J. van der Walt, et al. Array programming with NumPy, *Nature*. 585 (2020) 357–362. <https://doi.org/10.1038/s41586-020-2649-2>.
- [45] P. Virtanen, R. Gommers, T.E. Oliphant, et al. SciPy 1.0: fundamental algorithms for scientific computing in Python, *Nat. Methods*. 17 (2020) 261–272. <https://doi.org/10.1038/s41592-019-0686-2>.
- [46] P. Umesh, *Image Processing in Python*, *CSI Commun.* 23 (2012).
- [47] S. Evertz, S. Prünke, L. Patterer, A. Marshal, D.M. Holzapfel, A. Schökel, M. Hans, D. Primetzhofer, J.M. Schneider, Boron concentration induced Co-Ta-B composite formation observed in the transition from metallic to covalent glasses, *Condens. Matter*. 5 (2020). <https://doi.org/10.3390/condmat5010018>.
- [48] T.C. Hufnagel, U.K. Vempati, J.D. Almer, Crack-Tip Strain Field Mapping and the Toughness of Metallic Glasses, *PLoS One*. 8 (2013) e83289. <https://doi.org/10.1371/journal.pone.0083289>.
- [49] Y. Shi, M.L. Falk, Strain Localization and Percolation of Stable Structure in Amorphous Solids, *Phys. Rev. Lett.* 95 (2005) 095502. <https://doi.org/10.1103/PhysRevLett.95.095502>.